



# Efficiency of Cu and Pd substitution in Fe-based perovskites to promote N<sub>2</sub> formation during NH<sub>3</sub> selective catalytic oxidation (NH<sub>3</sub>-SCO)

Peixin Li<sup>a</sup>, Runduo Zhang<sup>a,\*</sup>, Ning Liu<sup>a</sup>, Sébastien Royer<sup>b</sup>

<sup>a</sup> State Key Laboratory of Chemical Resource Engineering, Beijing University of Chemical Technology, Beijing 100029 PR China

<sup>b</sup> Univ. Lille, CNRS, ENSCL, Centrale Lille, Univ. Artois, UMR 8181—UCCS—Unité de Catalyse et de Chimie du Solide, F-59000 Lille, France

## ARTICLE INFO

### Article history:

Received 8 July 2016

Received in revised form

30 September 2016

Accepted 8 October 2016

Available online 11 October 2016

### Keywords:

NH<sub>3</sub>-SCO

Perovskite

Mechanism

Palladium substitution

## ABSTRACT

Iron-based perovskites, of  $\text{LaFe}_{1-x}\text{B}'_{x}\text{O}_{3-\delta}$  ( $\text{B}' = \text{Cu, Pd}$ ) formula, are proposed as effective materials for the ammonia selective catalytic oxidation to nitrogen (NH<sub>3</sub>-SCO). Effects on N<sub>2</sub> yield, of copper or palladium substitutions in B position, and of perovskite dispersion over Al<sub>2</sub>O<sub>3</sub> support, are reported. Copper and palladium substitution in perovskite lattice significantly promotes the NH<sub>3</sub> conversion rate, owing to the outstanding redox capacity displayed by the substituted compositions at low temperature ( $T < 300^\circ\text{C}$ ). While N<sub>2</sub> yield decreases upon Cu-doping, it retains as high as 80–90% over Pd-containing catalysts. Copper substitution enhances low-temperature oxygen mobility, which is favorable to N–H bond fracture of adsorbed –ONH<sub>3</sub> species that results in high NO formation. Palladium substitution results in an opposite effect, and high selectivity towards N<sub>2</sub> is obtained. Additionally, N<sub>2</sub> yield is significantly improved at high temperature, when perovskite active phase is dispersed over Al<sub>2</sub>O<sub>3</sub> support. Combining *in-situ* DRIFTS and density functional theory (DFT) calculations, NH<sub>3</sub>-SCO to N<sub>2</sub> reaction pathway over Fe-based perovskites is proposed to follow an Eley-Rideal (E-R) mechanism, during which gaseous NH<sub>3</sub> reacts with adsorbed –ONH<sub>2</sub> species to form surface diazo species ( $-\text{N}=\text{N}-$ ). For LaFeO<sub>3</sub>, the rate-determining step is the –ON<sub>2</sub>H<sub>2</sub> to –ON<sub>2</sub>H reaction (overcoming an energy barrier of 3.48 eV), while for LaFe<sub>0.95</sub>Pd<sub>0.05</sub>O<sub>3</sub>, the rate-determining step is O–N bond cleavage (energy barrier of 1.55 eV) that explains then higher N<sub>2</sub> yield measured for the Pd-containing perovskite catalyst.

© 2016 Elsevier B.V. All rights reserved.

## 1. Introduction

Ammonia (NH<sub>3</sub>) is a widely used intermediate in major chemical processes, such as nitric acid and nitrogen fertilizer production plants, petroleum refining, and deNO<sub>x</sub> processes. Nevertheless, all these processes are plagued with ammonia slip phenomenon. Ammonia, with strong excitant odor, is one of the most significant N-containing gaseous pollutants for the environment. Different methods are proposed for NH<sub>3</sub> elimination: biological, chemical, physical, etc. [1] Selective catalytic oxidation of ammonia (NH<sub>3</sub>-SCO) in the presence of oxygen to produce harmless nitrogen and water presents the advantages of high efficiency and short response time. NH<sub>3</sub>-SCO is consequently considered as a technically and economically viable method for solving the problem of ammonia pollution. Recently, NH<sub>3</sub>-SCO reaction aroused extensive concern,

with different type of catalysts and reaction mechanisms proposed [2,3].

Active catalysts for the NH<sub>3</sub>-SCO reaction are among supported noble metal, zeolite and metal oxide. Supported noble metals are highlighted to be very efficient for this reaction, since the low temperature ( $<300^\circ\text{C}$ ).  $\gamma$ -Alumina supported platinum (2.6 wt.%) catalyst is reported active for the reaction, with N<sub>2</sub> yield as high as 82% at 270 °C, with reaction starting since 200 °C [4]. Li et al. [5] studied the properties of Ag/Al<sub>2</sub>O<sub>3</sub> catalyst for NH<sub>3</sub>-SCO reaction. It was proposed that well-dispersed and small Ag<sup>0</sup> particle enhanced catalytic activity. In the case of gold based catalyst, the presence of Au is reported to enhance amide-like ( $-\text{NH}_2$ ) and imido ( $-\text{NH}$ ) adspecies formation on the catalyst surface, species that are responsible for the improved SCO activity over such catalyst [6]. Some zeolite based catalysts, containing transition metal (TM), are also proposed as effective catalysts for this reaction. Long et al. [7] studied the influence of zeolite nature on catalytic properties of Fe-exchanged zeolites [Fe-ZSM-5 (MFI), Fe-mordenite (MOR) and Fe-clinoptilolite (HEU)]. The presence, in the solids, of mul-

\* Corresponding author.

E-mail address: [zhangrd@mail.buct.edu.cn](mailto:zhangrd@mail.buct.edu.cn) (R. Zhang).

multiple valent iron ions is beneficial to oxygen activation and thus results in high NH<sub>3</sub>-SCO performances over these kinds of materials. Due to adequate topology (stable crystal structure, excellent shape selectivity, and high Si/Al ratio), MFI-type iron-exchanged ZSM-5 presents high activity for the reaction, achieving 100% NH<sub>3</sub> conversion and 100% N<sub>2</sub> selectivity at 400–450 °C [8–10]. Besides, transition metal oxides such as CuO [11,12], Fe<sub>2</sub>O<sub>3</sub> [13], MnO<sub>2</sub> [14], MoO<sub>3</sub> [15], V<sub>2</sub>O<sub>5</sub> [16], CeO<sub>2</sub> [12,17], are also proposed for the reaction. However, they are significantly less active than supported noble metal catalysts and TM-exchanged zeolite-type catalysts. Recently, mixed-oxide formulations, including Ce-Zr-O [18], Ru-Cu-O [19], Ce-Ti-O [20], Cu-Ce-O [12,21], Mg-Al-O [22], as well as hydrotalcite-like [23,24] and spinel-like [25] materials, were also tested for the NH<sub>3</sub>-SCO reaction. Among them, catalysts containing copper [12,22,24,26] or palladium [27,28] are exhibiting high activity and selectivity to N<sub>2</sub>. The interaction of copper or palladium with other metal contained in the formulations, and modifications of material redox properties/oxygen mobility are proposed as the origin of the improved catalytic activities [29,30].

Simultaneously, NH<sub>3</sub>-SCO mechanism was also studied. Different mechanisms are proposed, depending on the nature of catalyst. Hydrazine (N<sub>2</sub>H<sub>4</sub>) is identified as an intermediate species during ammonia oxidation to N<sub>2</sub> over TiO<sub>2</sub>-supported catalyst. Yuan et al. [31] disclosed that hydrazine, which was identified as important intermediate species to generate N<sub>2</sub>, can be produced from NH<sub>3</sub><sup>+</sup> reacting with a second NH<sub>3</sub> molecule under oxygen limited conditions, and that NH<sub>3</sub><sup>+</sup> would react with O<sub>2</sub> to produce H<sub>2</sub>NO<sub>2</sub> species under excess oxygen conditions, which switches on the selective catalytic reduction (SCR) reaction (eventually leading to the formation of N<sub>2</sub> on V<sub>2</sub>O<sub>5</sub> material). Over Fe<sub>2</sub>O<sub>3</sub>-TiO<sub>2</sub> catalyst, *in-situ* DRIFTS measurements evidenced the formation of imido (–NH) and nitroxyl (–NO<sub>2</sub>) or hydroxylamine-type (NH<sub>2</sub>–OH) species during ammonia oxidation [32–34]. DFT calculations for the selective oxidation of ammonia on RuO<sub>2</sub> (1 1 0) suggest that the overall rate-determining step for NH<sub>3</sub> + O → NH + H<sub>2</sub>O has an energy barrier of 0.56 eV [35]. Besides, possible reaction pathways for the dehydrogenation of NH<sub>x</sub> species (x = 1–3) and the formation of the oxidation products of N<sub>2</sub>, NO, and H<sub>2</sub>O on Co<sub>3</sub>O<sub>4</sub> (1 0 0) [36] and Ir (1 0 0) [37] were proposed.

Perovskite solids with ABO<sub>3</sub> formula, having excellent thermal stability and satisfactory redox properties with the possibility to accommodate different cations in either A- and/or B- position [38], are widely used for exhaust gas treatment reactions, including deNO<sub>x</sub> [39–41], deN<sub>2</sub>O [42,43] and VOCs oxidation [44,45]. In LaFeO<sub>3</sub>, Fe<sup>3+</sup> partial substitution by Cu<sup>2+</sup> or by Pd<sup>2+</sup>, in B-sites induces greatly improved redox ability. Due to improved redox properties, these substituted solids present high activities for the NO + CO/C<sub>3</sub>H<sub>6</sub> reactions [46,47]. Unfortunately, perovskite-type oxides are mainly produced by crystallization at high temperature that is typically above 600 °C, which leads to materials with relatively low surface areas, and limited surface to bulk atom proportions. Dispersion of the perovskite over porous support is an efficient approach to limit the crystal domain growth occurring during calcination step. Various supports, exhibiting high surface areas and open porosities, are used among them ordered mesoporous silica [48–50], TiO<sub>2</sub>/CeO<sub>2</sub> [51], Al<sub>2</sub>O<sub>3</sub> [52,53], etc.

In this study, Fe-based perovskite-type oxides, where iron is partially substituted by Cu or Pd, are proposed as efficient catalysts for the selective catalytic oxidation of ammonia (NH<sub>3</sub>-SCO) to produce N<sub>2</sub>. The effect of Cu<sup>2+</sup> and Pd<sup>2+</sup> doping on the catalytic performance and N<sub>2</sub> selectivity of ferrite perovskite, as well as the impact of the dispersion of perovskite over an alumina support, are reported. Furthermore, *in-situ* DRIFTS analysis and DFT calculations are employed to reveal the NH<sub>3</sub>-SCO reaction mechanism, and to determine the rate-determining steps and possible intermediate

species that will further allow to improve catalytic performance by rational optimization of the catalyst formulation.

## 2. Experimental

### 2.1. Catalyst preparation

Bulk perovskite catalysts – LaFeO<sub>3</sub>, LaFe<sub>0.8</sub>Cu<sub>0.2</sub>O<sub>3</sub> and LaFe<sub>0.95</sub>Pd<sub>0.05</sub>O<sub>3</sub> – are prepared by high temperature pyrolysis, using citric acid as a complexation agent [54]. According to the 1:1 molar ratio of the A- and B-site cations, La(NO<sub>3</sub>)<sub>3</sub>·6H<sub>2</sub>O (99.0%) and Fe(NO<sub>3</sub>)<sub>3</sub>·9H<sub>2</sub>O (98.5%) are dissolved in 300 mL distilled water. For substituted solids, Cu(NO<sub>3</sub>)<sub>2</sub>·3H<sub>2</sub>O (99.5%) and Pd(NO<sub>3</sub>)<sub>2</sub>·2H<sub>2</sub>O (99.0%) are used as precursors. Subsequently, 100 mL of aqueous solution of citric acid, in order to achieve a molar ratio of citric acid to cation of 1, is slowly added to the precursor solution under stirring at 80 °C. Thereafter, the solution is maintained under stirring until a gel is obtained (5–6 h). Subsequently, the gel is transferred into an oven for drying at 100 °C during 24 h. The foam-like solid is finally calcined at 500 °C for 6 h (temperature increase rate of 5 °C min<sup>-1</sup>). LaFe<sub>0.8</sub>Cu<sub>0.2</sub>O<sub>3</sub>/Al<sub>2</sub>O<sub>3</sub> and LaFe<sub>0.95</sub>Pd<sub>0.05</sub>O<sub>3</sub>/Al<sub>2</sub>O<sub>3</sub> supported perovskites are produced by a modified citric acid complexation method. Difference consists in the impregnation of a known amount of Al<sub>2</sub>O<sub>3</sub> powder by the liquid complex phase, before increase of the solution viscosity. The loading of perovskite on Al<sub>2</sub>O<sub>3</sub> is ~40 wt.%. The ageing and thermal treatments applied are exactly similar to those applied for the crystallization of bulk materials.

### 2.2. Catalyst characterization

X-ray diffraction (XRD) patterns are collected over a Bruker D5005 diffractometer equipped with a Cu K $\alpha$  radiation ( $\lambda = 1.5406 \text{ \AA}$ ). Diffractograms are recorded with a 0.05° step scan (step time = 1 s) for the 2 $\theta$  range between 10° and 80°. Phase identification is performed by comparison with JCPDS database. Crystal domain sizes (D) are calculated using the Scherrer equation after Warren's correction for instrumental broadening.

The specific surface areas (S<sub>BET</sub>) are obtained by N<sub>2</sub> physisorption at –196 °C on a TRISTAR 3000 instrument from Micromeritics, using the Brunauer-Emmett-Teller (BET) method. Before analysis, samples are thermally treated under vacuum at 300 °C.

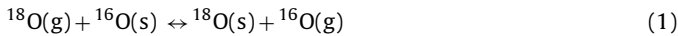
NH<sub>3</sub>-temperature programmed desorption (NH<sub>3</sub>-TPD) is performed on a Micromeritics AutoChem II 2920 instrument equipped with a thermal conductivity detector (TCD) for quantification. Approximately 100 mg of catalyst is pretreated at 500 °C under 5 vol.% O<sub>2</sub> in He flow (20 mL min<sup>-1</sup>) for 30 min, and then cooled down to 50 °C. The material is thereafter saturated with NH<sub>3</sub> at 50 °C for 1 h (4 vol.% NH<sub>3</sub> in He – 20 mL min<sup>-1</sup>). Thereafter, the loosely bonded ammonia is removed by flowing the solid under 20 mL min<sup>-1</sup> He (>99.999%) flow for 1 h. Finally, desorption is carried out from 50 °C to 500 °C at a heating rate of 10 °C min<sup>-1</sup> under He (20 mL min<sup>-1</sup>).

Temperature programmed reduction by H<sub>2</sub> (H<sub>2</sub>-TPR) is carried out on an AutoChem II 2920 instrument from Micromeritics. About 100 mg of catalyst is introduced in the microreactor and activated under simulated air (total flow rate = 50 mL min<sup>-1</sup>, at 500 °C for 1 h). After cooling down to 100 °C, the reducing flow (5 vol.% of H<sub>2</sub> in Ar) is stabilized at a total flow rate of 35 mL min<sup>-1</sup>, and the temperature of the reactor is increased from 100 °C to 500 °C (ramping rate = 5 °C min<sup>-1</sup>). The consumption of H<sub>2</sub> is on-line monitored by gas chromatography (GC, 4000A) equipped with a thermal conductivity detector (TCD).

The chemical states and atomic proportions of surface elements are evaluated by X-ray photoelectron spectroscopy (XPS) on a

Thermo-Fisher ESCALAB 250 system with Al  $K\alpha$  radiation under ultrahigh vacuum (UHV). The binding energy (BE) was calibrated with respect to the C1s value of carbon positioned at 285.0 eV.

Oxygen isotopic exchange and equilibration methods are generally used to evaluate oxygen mobility [29,55]. The exchange reaction mechanism can be described by the following equation:



where (s) and (g) refer to the solid and the gas phases, respectively. The experiments were carried out in a recycling U-shaped micro-reactor. The recirculation volume was coupled to a quadrupolar mass spectrometer (MQG Blazers). The gas sampling was regulated by a thermovalve adjusted to maintain a constant pressure of  $1 \times 10^{-6}$  mbar in the ionization chamber of the mass spectrometer. A constant mass of catalyst (0.050 g) was introduced in the reactor between two quartz wool plugs. For temperature-programmed exchange experiments,  $^{18}\text{O}_2$  was introduced at 200 °C, and the sample was heated up to 600 °C with a ramp of 2 °C min<sup>-1</sup>. In the case of the equilibration reaction, an equimolar volume of  $^{18}\text{O}_2$  and  $^{16}\text{O}_2$ , instead of pure  $^{18}\text{O}_2$ , was introduced in the reactor. The oxygen isotopic exchange results are presented in Section S5 in SI file.

### 2.3. Activity measurement

$\text{NH}_3$ -SCO catalytic tests are performed in a tubular quartz reactor (inner diameter 5 mm), in which is positioned 200 mg of catalyst. Reaction considered for the selective oxidation of  $\text{NH}_3$  to  $\text{N}_2$  is presented in Eq. (2):



The feed gas contains 0.1 vol.%  $\text{NH}_3$ , 0.15 vol.%  $\text{O}_2$ , in Ar (balance gas). The reaction is performed under a flow of 100 mL min<sup>-1</sup> (given a GHSV of 30,000 h<sup>-1</sup>). Concentrations in  $\text{NO}$ ,  $\text{NO}_2$ ,  $\text{N}_2\text{O}$  and  $\text{NH}_3$  in the inlet and outlet gases are measured using an IR gas analyzer IRAffinity-1, while  $\text{N}_2$  and  $\text{O}_2$  concentrations are monitored using gas chromatography (GC HP5890, equipped with a TCD and 5A molecular sieve and TDX-01 columns for product separations).

### 2.4. In-situ DRIFTS study

*In-situ* Diffuse Reflectance Infrared Fourier Transform Spectroscopy (DRIFTS) measurements are obtained on a TENSOR 27 instrument from BRUKER, equipped with a high sensitivity MCT detector and a diffuse reflection accessory including a high-temperature reaction chamber (Praying Mantis, Harrick). The catalyst (~50 mg) is ground and placed into the diffuse reflectance cell fitted with KBr windows positioned in a heating chamber that allows the temperature of sample to be stabilized at the desired temperature (150, 200, 250, and 300 °C). IR spectra are recorded by accumulating 64 scans at a spectra resolution of 4 cm<sup>-1</sup>, in the range of 600–4000 cm<sup>-1</sup>.  $\text{NH}_3$  and  $\text{O}_2$  concentrations used for *in-situ* experiments are 0.1 vol.% and 0.15 vol.%, respectively, in He.

### 2.5. Computational methods

Calculations are performed with the density functional theory (DFT) provided by the program DMol3 package. Spin-polarized calculations are employed using the generalized gradient approximation (GGA) with the Perdew-Burke-Ernzerhof (PBE) method to describe the exchange and correlation energy in all calculations. For geometry optimization, a  $1 \times 3 \times 1$  Monkhorst-Pack k-point mesh for the Brillouin zone sampling is used. Using periodic boundary, a plane-wave cutoff energy of 400 eV is employed. The  $\text{LaFeO}_3$  crystal with an orthorhombic perovskite structure *Pnma* (62) is calculated with 28 atoms in the unit cell. We explore possibility using a supercell ( $2 \times 2$ ), slab model of both  $\text{LaFeO}_3$  and  $\text{LaFe}_{0.95}\text{Pd}_{0.05}\text{O}_3$

perovskites terminated upon the most common (0 1 0) facet of the material. The energy of adsorption,  $E_{\text{ads}}$ , for the reactant molecules on the surface is defined in Eq. (3):

$$E_{\text{ads}} = E_{\text{adsorbate+surface}} - E_{\text{surface}} - E_{\text{gas}} \quad (3)$$

Where  $E_{\text{surface}}$  is the total clean relaxation energy of the surface slab,  $E_{\text{gas}}$  is the energy of the gas-phase adsorbate, and  $E_{\text{adsorbate+surface}}$  is the total energy of the system. Since the calculations are performed at 0 K and fixed cell volume, the differences in Gibbs free energy should equal the deviation in total energy. From this definition, a negative value of  $E_{\text{ads}}$  corresponds to an exothermic and spontaneous adsorption process.

To locate saddle points and establish reaction pathway, the climbing image – nudged elastic band (CI-NEB) method is used. This is a “chain of states” method, where several intermediate states or images of the system are connected by springs to map out a reaction pathway between an initial and a final state.

## 3. Results and discussion

### 3.1. Material structure and specific surface area

XRD patterns of bulk  $\text{LaFeO}_3$ ,  $\text{LaFe}_{0.8}\text{Cu}_{0.2}\text{O}_3$ , and  $\text{LaFe}_{0.95}\text{Pd}_{0.05}\text{O}_3$  perovskites, as well as of supported  $\text{LaFe}_{0.8}\text{Cu}_{0.2}\text{O}_3/\text{Al}_2\text{O}_3$  and  $\text{LaFe}_{0.95}\text{Pd}_{0.05}\text{O}_3/\text{Al}_2\text{O}_3$ , which are abbreviated as LaFe, LaFeCu, LaFePd, LaFeCu/ $\text{Al}_2\text{O}_3$  and LaFePd/ $\text{Al}_2\text{O}_3$ , are shown in Fig. S1. A comparison of these diffractograms with JCPDS references indicated that iron-based perovskite phase is successfully obtained for all materials. Indeed, copper and palladium containing bulk materials present comparable diffractograms than obtained for LaFe, with very slightly less intense contribution of the external lanthanum oxide phase for palladium containing material. For the LaFeCu/ $\text{Al}_2\text{O}_3$  material, the reflections attributed to the perovskite phase are detected in addition to poorly intense reflection attributed to aluminium oxide phase. The reflections of the perovskite phase are also easily detected for LaFePd/ $\text{Al}_2\text{O}_3$ , as for the bulk materials. This result suggests easy crystallization of the palladium-containing perovskite over alumina surface, as in the case of supported copper-containing material. Analysis of the diffraction patterns allows to calculate crystal domain sizes (Table 1). The crystal domain size follows the decreasing order: LaFePd (22.9 nm) > LaFePd/ $\text{Al}_2\text{O}_3$  (18.2 nm) > LaFe (12.7 nm) > LaFeCu (12.3 nm) > LaFeCu/ $\text{Al}_2\text{O}_3$  (12.1 nm). Discussion about crystal size for bulk and supported materials is given in Section S1 (XRD) of Electronic Supplementary file. TEM analysis confirms the formation of elementary particles of lower size in palladium-free solids (LaFe and LaFeCu) than for LaFePd (Section S4, ESI). Main conclusions are: (i) slightly larger crystal domain size is obtained over Pd-containing formulation, and (ii) based on XRD results, dispersion over a support has a limited effect on crystal domain size at the loading applied in this study.

The measured specific surface areas ( $S_{\text{BET}}$ ) are listed in Table 1. Bulk materials present moderate surface areas, ranging from  $15.5 \text{ m}^2 \text{ g}^{-1}$  (for LaFePd) to  $\sim 26 \text{ m}^2 \text{ g}^{-1}$  (for LaFe and LaFeCu). The specific surface areas displayed by LaFe and LaFeCu are almost equal, due to the formation of crystal of comparable size for the two materials. The lower surface area displayed by the palladium-containing material can be explained by the larger crystal domain size obtained after calcination. Compared with bulk perovskites, the specific surface areas displayed by the supported perovskites are slightly higher, with values comprised between  $31 \text{ m}^2 \text{ g}^{-1}$  (LaFeCu/ $\text{Al}_2\text{O}_3$ ) and  $45 \text{ m}^2 \text{ g}^{-1}$  (LaFeCu/ $\text{Al}_2\text{O}_3$ ). Such increase in surface area can be ascribed to the contribution of the support (60 wt.% of the total mass of catalyst) which is presenting initially a surface area of  $104 \text{ m}^2 \text{ g}^{-1}$ . To conclude, alumina supported perovskite

**Table 1**

Physical properties and  $\text{NH}_3$  desorption amounts obtained for bulk (LaFe, LaFeCu, LaFePd) and supported (LaFeCu/ $\text{Al}_2\text{O}_3$ , LaFePd/ $\text{Al}_2\text{O}_3$ ) perovskite samples.

Sample	Specific surface area ( $\text{m}^2 \text{g}^{-1}$ )	Cristal domain size (nm) <sup>a</sup>	Oxygen vacancy formation energy (eV) <sup>b</sup>	NH <sub>3</sub> desorption temperatures (°C)		Desorbed NH <sub>3</sub> amounts (mmol g <sup>-1</sup> )	
				First peak	Second peak	First peak	Second peak
LaFe	25.6	12.7	2.18	92	–	0.30	–
LaFeCu	25.9	12.3	1.85	92	–	0.29	–
LaFePd	15.5	22.9	3.06	95	185	0.37	0.04
LaFeCu/ $\text{Al}_2\text{O}_3$	44.8	12.1	–	95	198	0.38	0.07
LaFePd/ $\text{Al}_2\text{O}_3$	31.3	18.2	–	95	198	0.41	0.20

<sup>a</sup> Crystal domain size, obtained applying the Scherrer equation, after Warren's correction for instrumental broadening, on recorded diffractions patterns.

<sup>b</sup> Calculated using Eq. (4).

composites, having high surface areas, are obtained after calcination at 500 °C, with no evidence of significant single oxide phase formation over alumina. The perovskite particles formed over the support are suspected to present comparable crystalline properties, in composition and size, to the bulk ones.

### 3.2. NH<sub>3</sub>-TPD

During the NH<sub>3</sub>-SCO reaction, the adsorption of NH<sub>3</sub> is described as an important step [3,12,56]. Therefore, temperature programmed desorption of NH<sub>3</sub> (NH<sub>3</sub>-TPD) is often used to study surface ability of the material to adsorb NH<sub>3</sub>, and also allows to quantify surface acidity of solids. Amounts of ammonia desorbed below 500 °C over the synthesized solids are gathered in Table 1, with indicative temperatures of main (low temperature) and second (intermediate temperature) desorption peaks. The total amount of NH<sub>3</sub> desorption follows the order: LaFeCu (0.29 mmol g<sup>-1</sup>) ≈ LaFe (0.30 mmol g<sup>-1</sup>) < LaFePd (0.41 mmol g<sup>-1</sup>) < LaFeCu/ $\text{Al}_2\text{O}_3$  (0.45 mmol g<sup>-1</sup>) < LaFePd/ $\text{Al}_2\text{O}_3$  (0.61 mmol g<sup>-1</sup>). In all cases, the values obtained, below or equal to 0.61 mmol g<sup>-1</sup>, are relatively low if compared to classical acidic materials such as zeolites [57]. Comparable desorption profiles are obtained for all the tested materials, including the supported ones as shown in Fig. S2. The attribution of NH<sub>3</sub> desorption peaks is discussed in Section S2, with: (i) low temperature desorption originating from NH<sub>4</sub><sup>+</sup> species weakly bound to hydroxyl surface groups and possible desorption of residual physisorbed ammonia; (ii) intermediate temperature desorption originating from NH<sub>3</sub> coordinated to Lewis acid sites.

During NH<sub>3</sub>-SCO reaction, NH<sub>3</sub> is initially adsorbed on the oxide surfaces, before being subsequently transformed into NH<sub>x</sub> (x = 1,2) species [18,58]. Consequently, the transformation of adsorbed NH<sub>3</sub> species into surface NH<sub>x</sub> species is considered as a critical step in reaction process. Although the role of ammonia bonded to Brønsted acidic site (NH<sub>4</sub><sup>+</sup>) (low temperature) or Lewis acidic site (NH<sub>3</sub>) (moderate temperature) is still uncertain, it seems that ammonia adsorption mainly on Lewis acid sites appears to be the first step in NH<sub>3</sub>-SCO [20,32,59]. Amores et al. [32] supposes that Brønsted acidity is not required for NH<sub>3</sub>-SCO reaction. However, Zhang et al. suggested the need of both Lewis and Brønsted acidic sites, with a high ratio of Lewis to Brønsted site needed for the adsorption and activation of NH<sub>3</sub> over Mn-based perovskite [60].

In our cases, the shoulder peak at moderate temperature (185–200 °C), attributed to Lewis acid sites, is observed over LaFePd sample, while it is not observed over LaFe and LaFeCu bulk samples. Hence, adsorbed NH<sub>3</sub> would be most likely activated and further transformed into NH<sub>x</sub> on the surface of LaFePd sample due to its superior NH<sub>3</sub> adsorption capacity [20,32,59]. Alumina surface also presents Lewis acid sites [61]. Contribution from the support could arise in the low intensity shoulder peak, at around ~200 °C, over the two supported materials (LaFeCu/ $\text{Al}_2\text{O}_3$ , LaFePd/ $\text{Al}_2\text{O}_3$  – Table 1). Consequently, supporting the perovskite on alumina could favor of

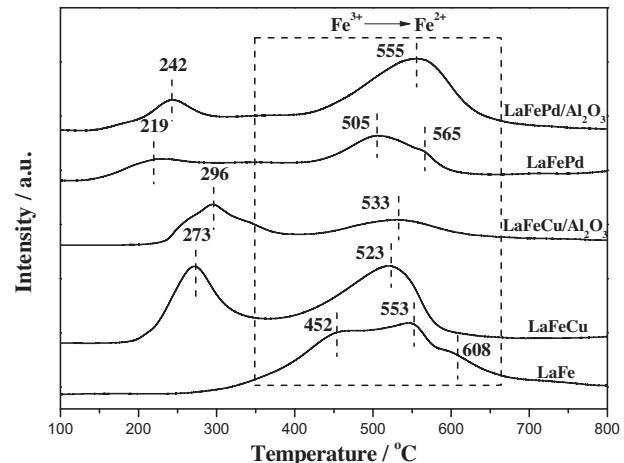


**Fig. 1.** H<sub>2</sub>-TPR profiles recorded for bulk (LaFe, LaFeCu, LaFePd) and supported (LaFeCu/ $\text{Al}_2\text{O}_3$ , LaFePd/ $\text{Al}_2\text{O}_3$ ) perovskite samples.

NH<sub>3</sub> activation step if surface sites from the support can participate to the reaction process.

### 3.3. H<sub>2</sub>-TPR

Temperature programmed reduction profiles are shown in Fig. 1, and amounts of hydrogen consumed at each reduction step are gathered in Table 2. For LaFe sample, a broad reduction peak from 350 °C to 670 °C, composed by a minimum of three distinct processes, is observed. The first peak located at 452 °C and second peak located at 553 °C and above are, as accepted in the literature [29,30], ascribed to successive reduction of Fe<sup>3+</sup> to Fe<sup>2+</sup> from surface and bulk, respectively. This interpretation is confirmed by the evaluation of the fraction of Fe<sup>3+</sup> reduced to Fe<sup>2+</sup> at the end of reduction, taking into account the amount of hydrogen consumed during this step (Table 2). Indeed, amount of H<sub>2</sub> consumed corresponds to a reduction limited to 41.0% of the Fe<sup>3+</sup> to Fe<sup>2+</sup>.

Cu-substituted materials present significantly different reduction profiles. A reduction peak appears at relatively low temperature. For LaFeCu sample, an apparent broad peak at 273 °C is observed. It is ascribed to Cu<sup>2+</sup> → Cu<sup>0</sup> reduction, according to the literature [29], and confirmed by the amount of hydrogen consumed at this step that gives a reduction of 63.0% of Cu<sup>2+</sup> to Cu<sup>0</sup> (Table 2). Over the LaFeCu/ $\text{Al}_2\text{O}_3$  sample, the low temperature reduction peak is slightly shifting to higher temperature (296 °C). Taking into account the perovskite loading, the amount of H<sub>2</sub> consumption, calculated reduction degree of Cu<sup>2+</sup> to Cu<sup>0</sup> is 95.1%, supporting that this hydrogen consumption is related to the reduction of cationic copper to metal. Over these two materials, a reduction is also observed between 400 °C and 600 °C, with temperatures comparable to those measured for LaFe. It corresponds

**Table 2**

Temperature Programmed Reduction characteristics obtained for the different materials.

Sample	Experimental H <sub>2</sub> consumption <sup>a</sup> (mmol g <sup>-1</sup> )		Theoretical H <sub>2</sub> consumption <sup>b</sup> (mmol g <sup>-1</sup> )			Experimental cation reduction degree <sup>c</sup> (%)		
	Low T (150–350 °C)	High T (350–670 °C)	Cu <sup>2+</sup> → Cu <sup>0</sup>	Pd <sup>2+</sup> → Pd <sup>0</sup>	Fe <sup>3+</sup> → Fe <sup>2+</sup>	Cu	Pd	Fe
LaFe		0.837	–	–	2.034	–	–	41.0
LaFeCu	0.515	0.650	0.818	–	1.636	63.0	–	39.7
LaFeCu/Al <sub>2</sub> O <sub>3</sub> <sup>d</sup>	0.311	0.186	0.327	–	0.654	95.1	–	28.4
LaFePd	0.145	0.445	–	0.103	1.959	–	>100 <sup>e</sup>	24.9
LaFePd/Al <sub>2</sub> O <sub>3</sub> <sup>d</sup>	0.133	0.674	–	0.041	0.783	–	>100 <sup>e</sup>	97.8

<sup>a</sup> Mole of H<sub>2</sub> consumed per gram of materials, issued from H<sub>2</sub>-TPR experiment.<sup>b</sup> Theoretical values of H<sub>2</sub> to be consumed to achieve a complete reduction of the different cations in the analyzed materials (reduction reactions depicted in the table).<sup>c</sup> Cation reduction degrees obtained experimentally.<sup>d</sup> Theoretical H<sub>2</sub> consumption of supported materials (LaFeCu/Al<sub>2</sub>O<sub>3</sub> and LaFePd/Al<sub>2</sub>O<sub>3</sub>) being equal to 40% of that of non-supported materials with neglecting aluminium cation.<sup>e</sup> >100 indicates that the experimental H<sub>2</sub> consumption exceeds the theoretical value to completely reduce the cation. Excess of H<sub>2</sub> consumed is added to the amount obtained for the Fe<sup>3+</sup> to Fe<sup>2+</sup> reduction step.

to the reduction of a limited fraction of surface and bulk Fe<sup>3+</sup> into Fe<sup>2+</sup> (39.7% and 28.4%, Table 2).

Comparable evolution of the reduction profiles is observed over the Pd-containing catalysts. A small content in Pd<sup>2+</sup> also improves reducibility at low temperature. The first reduction peak is observed located at 219 °C (LaFePd) and 242 °C (LaFePd/Al<sub>2</sub>O<sub>3</sub>). Taking into account the content of palladium in the solids and the amounts of H<sub>2</sub> consumed, this peak is attributed to the Pd<sup>2+</sup> → Pd<sup>0</sup> reduction process (with values of palladium reduction to metal calculated at 100%, for LaFePd and LaFePd/Al<sub>2</sub>O<sub>3</sub>), with the starting of Fe<sup>3+</sup> to Fe<sup>2+</sup> reduction (since hydrogen consumption exceeds the amount to entirely reduce the palladium into metal). Reduction of palladium is then observed to occur at a slightly lower temperature (about 50–60 °C) than copper. A high-temperature reduction is also observed for these materials, always attributed to the reduction of trivalent iron into divalent iron. Proportion of iron reduction (Table 2) is also affected by the presence of the support, with reduction degree from 24.9% (LaFePd) to 97.8% (LaFePd/Al<sub>2</sub>O<sub>3</sub>), when excess of H<sub>2</sub> consumed during the first step is added to consumption of the second step.

### 3.4. XPS

Fe 2p<sub>3/2</sub> and O 1s spectra obtained for the different samples are presented in Fig. 2, with relative surface concentration being gathered in Table 3. Fig. 2(a) presents the Fe 2p<sub>3/2</sub> spectra obtained for the different materials. A first contribution, around 709.8 eV, and a second contribution, around 711.1 eV, are seen. They are attributed to Fe<sup>2+</sup> and Fe<sup>3+</sup> on the crystal surface, respectively [62]. Over LaFe, most of the iron is in the +III valence with a Fe<sup>3+</sup>/Fe<sup>2+</sup> ratio equal to 7.9. The iron substitution by lower valence copper or palladium results in very limited decrease of this ratio. This result implies that there could be surface electron transfer from copper or palladium atoms to iron atoms, which results in a conversion of Fe<sup>3+</sup> surface sites into Fe<sup>2+</sup> surface sites. Comparison between bulk (ICP) and surface (XPS) Fe/La atomic ratio shows a surface enrichment in lanthanum as always reported for LaFeO<sub>3</sub> perovskites. In addition, atomic ratio suggests the segregation of B' substituents on perovskite surface (SI file, XPS section), with a more marked palladium surface segregation than copper surface segregation.

O 1s spectra are presented in Fig. 2(b). Three contributions – around 529.5 eV, 531.2 eV, and 532.3 eV – are observed. These three contributions refer to: crystal lattice oxygen ions (O<sup>2-</sup>, 529.5 eV), chemically adsorbed surface oxygen species (O<sub>2</sub><sup>-</sup> or O<sup>-</sup>, 531.2 eV), and hydroxyl and carbonate oxygen species (OH<sup>-</sup>, CO<sub>3</sub><sup>2-</sup>, 532.3 eV) [63]. Calculated O<sub>ads</sub>/O<sub>total</sub> atomic ratios issued from the contribution of each oxygen species are presented in Table 3. Incorporation of copper and palladium in the formulation results in slightly higher

O<sub>ads</sub>/O<sub>total</sub> ratio (0.54) [64], while apparently lower ratio (0.33) is obtained upon palladium incorporation [65]. Consequently, copper substitution seems to be more adequate to promote the formation of surface vacancies [66] that are available for adsorption and dissociation of gaseous dioxygen molecule on its surface. Yang et al. demonstrated that iron substitution by copper significantly promoted either surface or bulk oxygen mobility, which is in line with results obtained here suggesting the formation of higher density in surface vacancies in Cu-substituted materials (needed for gas phase molecule adsorption – dissociation – exchange) [29]. Contrarily, Pd-substitution seems to cause a decrease of surface sites for gaseous molecule adsorption and dissociation, characterized by lower surface O<sub>ads</sub>/O<sub>total</sub> ratio. This result is coherent with trend reported by Li et al. who pointed out that material with palladium in the lattice shows stronger intensity of lattice oxygen photo-peaks [65]. Also, Yang et al. [29] demonstrated that a decrease in surface oxygen mobility is observed when palladium substitutes iron in perovskite structure, an observation that is in line with the experimental evolution in O<sub>ads</sub>/O<sub>total</sub> ratio from this study. Results of temperature programmed <sup>18</sup>O isotopic exchange reaction, performed for the three bulk materials, confirm the beneficial effect of Cu-substitution, and the negative effect of Pd-substitution, on the perovskite oxygen mobility (Figs. S4 and S5). A depressed oxygen mobility is expected to be beneficial to limited oxidation of nitrogen atom, and consequently to limited production of high N-valence products such as N<sub>2</sub>O, NO, and NO<sub>2</sub> [67].

### 3.5. Activity test

Catalytic performances of catalysts for the selective catalytic oxidation of ammonia (NH<sub>3</sub>-SCO) are shown in Fig. 3. NH<sub>3</sub> conversion and N<sub>2</sub> yield obtained over LaFeO<sub>3</sub> sample, at different oxygen concentrations, are presented in Fig. 5(a and b). As observed in Fig. 3(a), NH<sub>3</sub> conversion starts between 150 °C and 200 °C, and increases up to a value of above 90% at T > 450 °C except at low O<sub>2</sub> concentration (750 ppm). Conversion is significantly affected by the oxygen concentration in the feed. Comparable activity is obtained for O<sub>2</sub> concentration of 3000 ppm and 5000 ppm. Activity is significantly depressed by decreasing the oxygen concentration below 3000 ppm (750 ppm and 1500 ppm). Then, with concentration of 750 ppm of O<sub>2</sub>, conversion starts at 200 °C and hardly achieves 80% at 600 °C. Concerning N<sub>2</sub> yield, an opposite trend is observed, with an increase in N<sub>2</sub> yield associated with a decrease in O<sub>2</sub> concentration. The effect of oxygen concentration is especially visible at high conversion, with N<sub>2</sub> yield varying from 72% (at 450 °C with 750 ppm of O<sub>2</sub>) to 38% (at the same temperature with 5000 ppm O<sub>2</sub>). Consequently, a high O<sub>2</sub> concentration, even if favorable to NH<sub>3</sub>

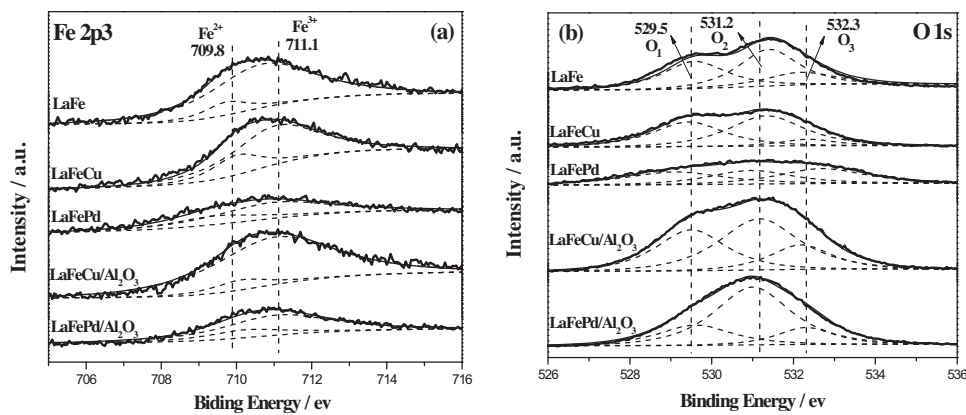


Fig. 2. XPS pattern of (a) Fe 2p and (b) O 1s for as-prepared samples; in O 1s spectra: lattice oxygen ( $O_1$ ), adsorbed oxygen ( $O_2$ ), and hydroxyl/carbonate ( $O_3$ ).

**Table 3**  
Surface element concentrations obtained by XPS for the different materials.

Sample	Surface concentrations (at.%)						surface element atomic ratio <sup>a</sup>				
	La 3d5	Fe 2p3	Cu 2p3	Pd 3d	Al 2p	O 1s	XPS Fe/La	Bulk Fe/La	XPS B'/Fe <sup>b</sup>	Bulk B'/Fe <sup>b</sup>	$O_{ads}/O_{tot}^c$
LaFe	12.6	6.8	–	–	–	80.6	0.54	1	–	–	0.52
LaFeCu	12.5	6.6	2.2	–	–	78.7	0.53	0.8	0.33	0.25	0.54
LaFePd	11.8	5.8	–	0.8	–	81.6	0.49	0.95	0.14	0.05	0.33
LaFeCu/Al <sub>2</sub> O <sub>3</sub>	8.2	3.0	1.2	–	25.0	62.6	0.37	0.8	0.40	0.25	–
LaFePd/Al <sub>2</sub> O <sub>3</sub>	6.1	2.4	–	0.3	28.0	63.2	0.39	0.95	0.13	0.05	–

<sup>a</sup> Surface relative abundance of each elements, obtained by decomposition of XPS signals.

<sup>b</sup> B' cation is Cu<sup>2+</sup> or Pd<sup>2+</sup>.

<sup>c</sup>  $O_{tot}$ , total oxygen obtained by summing  $O_1$ ,  $O_2$  and  $O_3$  species of the O 1s spectra.

conversion, induces a decrease in N<sub>2</sub> selectivity with pronounced formation of NO<sub>x</sub> molecules (not shown).

Catalytic results obtained over LaFe, LaFeCu, LaFePd are compared in Fig. 3(c–e). ESI file presented the evolution of the catalytic properties of palladium-containing perovskite. Fig. S7 shows that the LaFePd presented here, with a composition of LaFe<sub>0.95</sub>Pd<sub>0.05</sub>O<sub>3±δ</sub>, is presenting the best compromise in terms of conversion and N<sub>2</sub> yields among the series (with atomic substitution degree from 0.02 to 0.1).

For LaFeCu, NH<sub>3</sub> conversion occurs at lower temperature than that does over LaFe. Comparable evolution in activity was observed for CO oxidation, and was related to the increase in oxygen mobility upon copper incorporation in perovskite lattice [29]. LaFePd presents a moderate activity, between that of LaFeCu and that of LaFe. Conversion is observed between 5% and 20% at the temperature below 200 °C due to the NH<sub>3</sub> adsorption and conversion at oxygen vacancies generated by Cu or Pd substitution. It increases significantly for temperature between 200 °C and 350 °C, and NH<sub>3</sub> conversion tends to be stable at conversion of 90–100% at temperatures above 350 °C (LaFeCu) and 450 °C (LaFe). N<sub>2</sub> yield for the Cu-doped and Pd-doped materials is between 5% and 20% at temperature below 200 °C. NH<sub>3</sub> catalytic oxidation at low temperature is consequently observed to be fully selective to N<sub>2</sub> over these materials (zone of low conversion, <20%). As the temperature increases, differences in N<sub>2</sub> yields are observed between the solids. For LaFe, N<sub>2</sub> yield gradually increases from 200 °C to 400 °C, up to 50–55%. A comparable evolution of the NO yield is observed, with progressive increase followed by stabilization at a yield of ~40% (Fig. 3(e)). For LaFeCu sample, N<sub>2</sub> yield sharply increases between 200 °C and 250 °C, to reach a yield as high as 75% at 250 °C. Unfortunately, N<sub>2</sub> yield is found to rapidly decrease upon further temperature increase, to stabilize at ~40% at temperature above 450 °C. The decline in N<sub>2</sub> yield is associated with

an increase in NO yield which is observed to increase and finally stabilizes around 60% (20% higher than that of LaFe – Fig. 3(e)). The high oxygen mobility, surface and bulk, of copper-substituted perovskite, originating from significant vacancy densities [46,47], could be at the origin of the significant increase in NO yield over the copper-based material, confirming a high ability of copper-containing perovskites for low-temperature oxidation reactions. This is also the only solid for which NO<sub>2</sub> is detected, even if the concentration always remains low (below 10 ppm, in the temperature range 450–600 °C). For LaFePd sample, the N<sub>2</sub> yield increased from ~20% at 200 °C to 80–90% at 300 °C. Comparable value of N<sub>2</sub> yield is maintained even upon temperature increases up to 600 °C, with no significant modification in NO yield that is observed to fluctuate around 15–20% between 300 °C and 600 °C (Fig. 3(e)). For this solid, NO<sub>2</sub> formation is not observed in the tested temperature range, while only a little N<sub>2</sub>O (<5 ppm) is observed in the 250–450 °C temperature range. This result is significantly different from this obtained for LaFeCu, during which important decrease in N<sub>2</sub> yield is observed in this temperature range, with significant formation of NO and detection of ppm production of NO<sub>2</sub> at elevated temperature. Then, palladium containing formulations are more adapted than copper ones to produce N<sub>2</sub>, especially at high temperatures. This result does not directly correlate with results obtained by TPR (Fig. 1) for which the temperature of palladium reduction is observed at slightly lower temperature than copper reduction that could presume of a better oxidation ability. However, it correlates perfectly with our precedent results [29] for which oxygen mobility measurements and CO/CH<sub>4</sub> oxidation experiments showed that Pd-containing formulations present lower oxidation ability than Cu-containing formulation, despite low-temperature reducibility of palladium observable by TPR. Inhibition of oxygen mobility (surface and bulk) by palladium stabilization in/over the perovskite structure is proposed to be at the origin of this evolu-

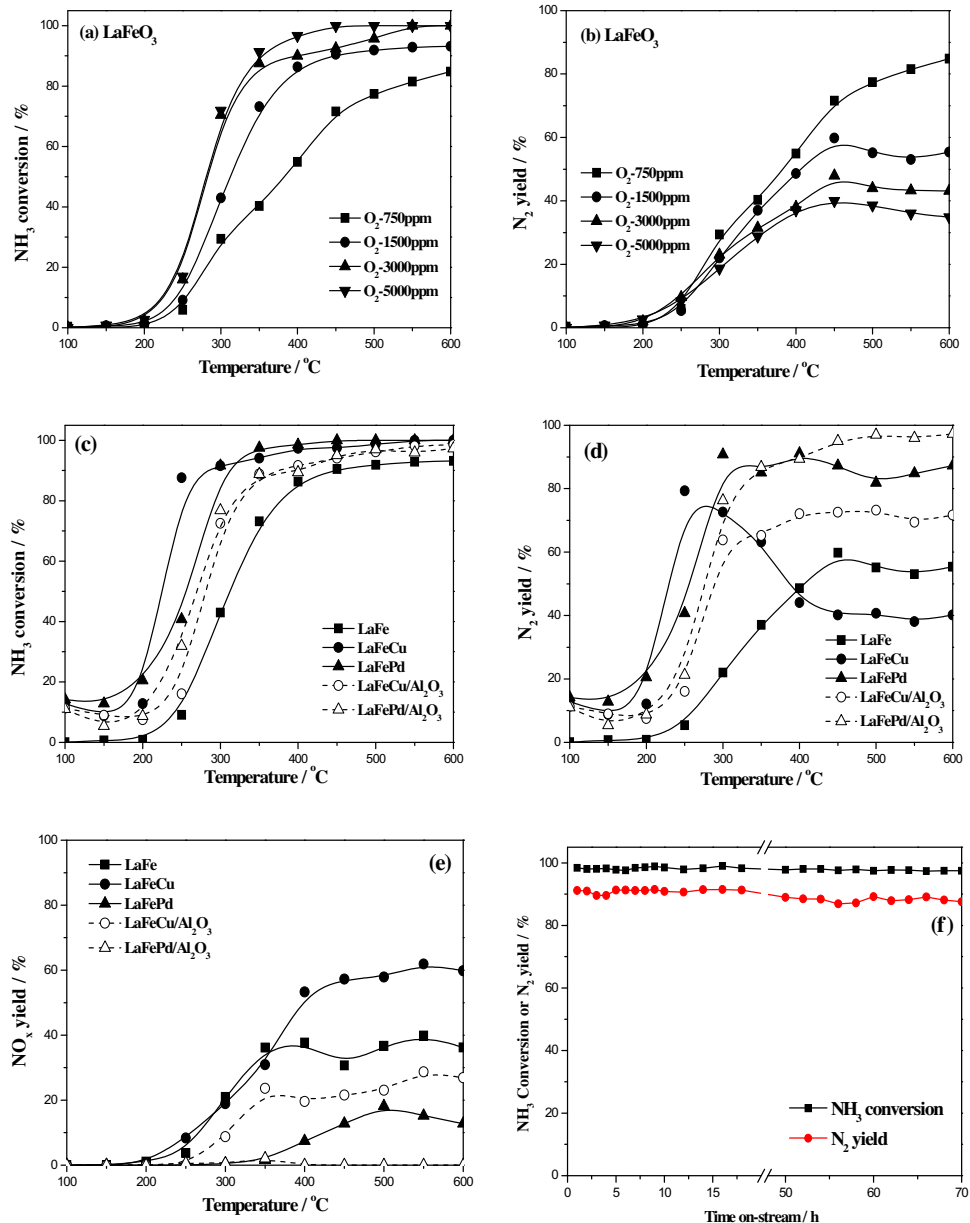


**Fig. 3.** Catalytic performance of perovskite for NH<sub>3</sub>-SCO: (a and b), effect of O<sub>2</sub> concentration on NH<sub>3</sub> conversion and N<sub>2</sub> yield over LaFeO<sub>3</sub>; (c–e) NH<sub>3</sub> conversion, N<sub>2</sub> yield, and NO yield over bulk (LaFe, LaFeCu, LaFePd) and supported (LaFeCu/Al<sub>2</sub>O<sub>3</sub>, LaFePd/Al<sub>2</sub>O<sub>3</sub>) perovskite samples; (f) Long-term stability test for LaFePd at 400 °C. Reaction conditions: 0.1 vol.% NH<sub>3</sub>, 0.15 vol.% O<sub>2</sub> in Ar at a total flow rate of 100 mL min<sup>-1</sup> (GHSV = 30,000 h<sup>-1</sup>).

tion. As a remarkable result here is consequently the low light-off temperatures recorded for NH<sub>3</sub> oxidation (<300 °C), and the maintain of high selectivity to N<sub>2</sub> even when temperature increases up to 600 °C, obtained over the Pd-containing perovskite.

The properties of the bulk materials are compared with those of the supported derived materials. A slight shift of the conversion curves toward the higher temperatures is observed over supported catalysts. NH<sub>3</sub> conversion of ~88% is achieved at temperature around 350 °C for supported perovskites, while bulk materials present conversions from 92% (LaFeCu) to 96% (LaFePd) at comparable temperature. This decrease in conversion rate over the supported perovskite (Fig. 3(c)) is originating from the lower content of perovskite in the reactor when supported catalysts are studied (the perovskite phase contributes to only 60 wt.% of total weight of the catalyst). The poor activity of the alumina explains why the global catalyst activity is observed to slightly decrease (Fig. S6) for supported catalysts. However, the activities achieved over

the two supported materials exceed that achieved over bulk LaFe, showing the good performances of these two supported materials despite the significantly lower perovskite content in the reactor. N<sub>2</sub> yields, for LaFeCu/Al<sub>2</sub>O<sub>3</sub> and LaFePd/Al<sub>2</sub>O<sub>3</sub>, remain below those obtained for the bulk sample, when temperature of reaction stays below 350 °C. However, these two supported solids present N<sub>2</sub> yields higher than those of bulk solids when temperature increases above 350 °C. For LaFeCu/Al<sub>2</sub>O<sub>3</sub>, yield stabilizes at ~70% (T > 350 °C), while for LaFePd/Al<sub>2</sub>O<sub>3</sub>, yield increases monotonously from 86% (T = 350 °C) to ~95% (T = 450 °C and higher). A remarkable result concerns the supported palladium containing perovskite, for which almost no NO<sub>x</sub> is produced whatever the reaction temperature (from 200 °C to 600 °C) while the Pd-containing bulk material leads to NO yields of 8%–18% in the 400–600 °C region. The selectivity in N<sub>2</sub> during NH<sub>3</sub>-SCO reaction is then positively affected by dispersing perovskite phase on alumina support. Temperature programmed reduction (Fig. 1) showed, for LaFePd/Al<sub>2</sub>O<sub>3</sub>, a shift of the

reduction peaks ( $\text{Pd}^{2+} \rightarrow \text{Pd}^0$ ;  $\text{Fe}^{3+} \rightarrow \text{Fe}^{2+}$ ) towards higher temperatures. Comparable observation was performed for Cu-containing perovskite. Such evolution indicates a decrease in perovskite B-cation reducibility when perovskite is dispersed over alumina, and could be explained by strong interaction between perovskite and support surface [52,68]. Besides, XPS results also support the formation of strong interaction between perovskite and  $\text{Al}_2\text{O}_3$  surface. This interaction can result in a depressed oxidation ability in the final material, with, as a consequence, a decrease in high oxidation state N compounds formation in favor to the formation of less oxidized  $\text{N}_2$ . Then, the dispersion of perovskite (containing either Cu or Pd) over alumina is beneficial to the formation of  $\text{N}_2$  (higher  $\text{N}_2$  yield than obtained over bulk catalysts) rather than the formation of more oxidized compounds ( $\text{NO}_x$ ), due to the decrease of perovskite phase oxidation ability when supported over alumina.

These results, especially those reported for the supported and unsupported palladium containing perovskites, are among the best in terms of  $\text{N}_2$  yields when compared with performances reported over optimized systems, including other mixed-oxide formulations and noble metal based catalysts, presented in the recent literature (Table S1). Adequate optimization of the perovskite oxidation ability is, through perovskite composition modulation, a judicious way to design efficient perovskite-based catalyst for  $\text{NH}_3$ -SCO reaction.

Finally, considering the good performances of the proposed systems and aiming at practical applications, a long-term reaction for evaluating stability is performed over LaFePd sample (at 400 °C). As shown in Fig. 3(f),  $\text{NH}_3$  conversion and  $\text{N}_2$  yield respectively remains at ~98% and ~90% during the 70 h of reaction. This result clearly indicates that the LaFePd sample, which presents excellent catalytic properties, is also stable under reaction and does not suffer from dramatic deactivation.

### 3.6. $\text{NH}_3$ -SCO mechanism over palladium containing perovskite

Mechanism of ammonia selective catalytic oxidation ( $\text{NH}_3$ -SCO), to generate dinitrogen through hydrazine ( $\text{N}_2\text{H}_4$ ) intermediate under lean oxygen concentration was previously reported [5,31,59,69]. In addition, the “internal” selective catalytic reduction (iSCR) mechanism consisting in first oxidation of  $\text{NH}_3$  to NO followed by its reduction by unreacted  $\text{NH}_3$  under rich oxygen concentration was also announced [13,70,71].

#### 3.6.1. Case of $\text{LaFeO}_3$

$\text{LaFeO}_3$  is active in the 150–300 °C temperature range, with  $\text{N}_2$  yield reaching 40% at 300 °C. *In-situ* DRIFTS experiments are carried out, for LaFe, between 150 °C and 300 °C (Fig. 4(a)).

**3.6.1.1. At low temperature (150 °C).** Bands located at 930  $\text{cm}^{-1}$  and 965  $\text{cm}^{-1}$ , attributed to gaseous  $\text{NH}_3$ , are observed in Fig. 4(a). The existence of adsorbed  $\text{NH}_3$  species is evidenced by the bands appearing at 1625, 1692, 3155, 3253, and 3338  $\text{cm}^{-1}$ . Signals at 3155, 3253, and 3338  $\text{cm}^{-1}$  are attributed to stretching vibration of N–H bonds in coordinated  $\text{NH}_3$ . Signals at 1625 and 1692  $\text{cm}^{-1}$  are assigned to the stretching vibration of  $\text{NH}_3$  on Lewis acid sites and  $\text{NH}_4^+$  species on Brønsted acid sites, respectively [72]. Interestingly, the band belonging to Lewis acidic sites (coordinated  $\text{NH}_3$ ) at 1625  $\text{cm}^{-1}$  is stronger than that of Brønsted acidic sites (in the form of  $\text{NH}_4^+$ ), indicating  $\text{NH}_3$  is inclined to adsorb at Lewis acidic site. Additional signals at 1291, 1560, and 1588  $\text{cm}^{-1}$ , corresponding to  $-\text{NH}_2$  scissoring,  $-\text{NH}_2$  deformation vibration and  $\text{NH}_2$  wagging of hydroxylamine species ( $\text{NH}_2\text{O}$ –) [32,34], are also detected. In addition, a flat band with low intensity is observable at 1179  $\text{cm}^{-1}$ , and corresponds to N–N stretching, indicating minor amount of  $\text{N}_2\text{H}_x$  is present at 150 °C. Small signal is also detected for adsorbed nitrate species, at 1548  $\text{cm}^{-1}$ . There-

fore,  $\text{NH}_3$  could be adsorbed on acidic sites to produce intermediate  $-\text{NH}_2$  species, inducing a reaction even at low temperature.

**3.6.1.2. From 200 °C to 300 °C.** As the temperature increases, the band at 1588  $\text{cm}^{-1}$ , attributed to  $-\text{NH}_2$  scissoring is significantly enhanced. Relative intensity of bands located at 1179 and 1291  $\text{cm}^{-1}$ , respectively assigned to N–N stretching and  $-\text{NH}_2$  wagging, also increases. In addition, another signal, at 1332  $\text{cm}^{-1}$  and attributed to  $-\text{NH}_2$  wagging, appears for temperature higher than 250 °C [32]. Contrarily, no notable change in intensity can be observed for adsorbed nitrate species (1548  $\text{cm}^{-1}$ ), and no other signal for nitrite/nitrate species can be detected. Consequently, gaseous  $\text{NH}_3$  adsorbs on either Brønsted sites (in the form of  $\text{NH}_4^+$ ) or Lewis sites (coordinated  $\text{NH}_3$ ) to form adsorbed  $\text{NH}_3$ , and then undergoes partial dehydrogenation to obtain stable  $\text{NH}_2$  intermediate. Subsequently,  $\text{NH}_2$  dimerizes on the surface with further dehydrogenation to form  $\text{N}_2\text{H}_x$  species.

#### 3.6.2. Case of $\text{LaFe}_{0.95}\text{Pd}_{0.05}\text{O}_3$

LaFePd presents the best catalytic performances, with low light-off temperature and high selectivity in  $\text{N}_2$  maintained even at high  $\text{NH}_3$  conversion.

**3.6.2.1. At low temperature (150 °C).** In Fig. 4(b), bands for gaseous  $\text{NH}_3$  (930, 965  $\text{cm}^{-1}$ ) and adsorbed  $\text{NH}_3$  species (1120, 1623, 1650, 1692, 3155, 3253, 3334  $\text{cm}^{-1}$ ) are observed. The bands observed from 3000 to 3500  $\text{cm}^{-1}$  are ascribed to stretching vibration of N–H bonds, while the bands at 1623  $\text{cm}^{-1}$  and 1692  $\text{cm}^{-1}$  likewise belong to  $\text{NH}_3$  on Lewis acid sites and  $\text{NH}_4^+$  on Brønsted acid sites, respectively. The shoulder band, at 1650  $\text{cm}^{-1}$ , originates from symmetric deformation vibration of  $\text{NH}_4^+$  species. These results suggest that  $\text{NH}_3$  adsorbs over Brønsted and Lewis sites, like over unsubstituted LaFe sample. Signals located at 1050–1160  $\text{cm}^{-1}$  are attributed  $\text{NH}_2$  rocking, and the band at around 1560  $\text{cm}^{-1}$  originates from the asymmetric deformation vibration ( $\delta_{\text{asy}}$ ,  $\text{NH}_2$ ) [6,33], which illustrates the first cleavage of N–H bond that occurs even at low temperature (150 °C). A weak band, at 1302  $\text{cm}^{-1}$ , is also observed and attributed to surface bidentate nitrate surface species.

**3.6.2.2. From 200 °C to 300 °C.** As temperature rises, the bands attributed to acid site adsorbed  $\text{NH}_3$  ( $\text{NH}_4^+$  and coordinated  $\text{NH}_3$ ) remain significant while they were observed to obviously decrease in relative intensity over LaFe does. This evolution indicates that LaFePd possesses higher  $\text{NH}_3$  adsorption ability than LaFe, which is in accordance with the results of  $\text{NH}_3$ -TPD (for which higher amount of ammonia was observed to be desorbed from the palladium-containing solid). Bands at 1050–1160  $\text{cm}^{-1}$ , attributed to  $\text{NH}_2$  rocking, and band at 1560  $\text{cm}^{-1}$  ( $\delta_{\text{asy}}$ ,  $\text{NH}_2$ ), are remaining at temperatures above 150 °C. In addition to the band of 1302  $\text{cm}^{-1}$  observed at 150 °C (bidentate nitrate species), bands at 1508 and 1543  $\text{cm}^{-1}$ , attributed to chelating bidentate nitrate [47,51,73] are identified at higher temperatures. The relative intensities of these two bands are low, which suggests only small fraction of ammonia oxidized into nitrate species on the material surface. Some new bands, located at 1177–1179, 1267, and 1590  $\text{cm}^{-1}$ , also appear above 200 °C, with their relative intensities increasing with temperature. Among them, the band located at 1267  $\text{cm}^{-1}$  is assigned to  $\text{NH}_2$  wagging modes in  $\text{NH}_2\text{O}$ – species. This result illustrates the formation of hydroxylamine surface species ( $\text{NH}_2\text{O}$ –), occurring through reaction with surface oxygen species [34]. Bands at 1177, 1179 and 1590  $\text{cm}^{-1}$  are assigned to the  $\text{NH}_2$  scissoring, N–N stretching and  $\text{NH}_2$  rocking, respectively. In addition, a minor band at 1416  $\text{cm}^{-1}$  attributed to the imido (-NH) species, following  $\text{N}_2\text{H}_x$  formation, is also detected [6]. Therefore, the oxidation of  $\text{NH}_3$  over

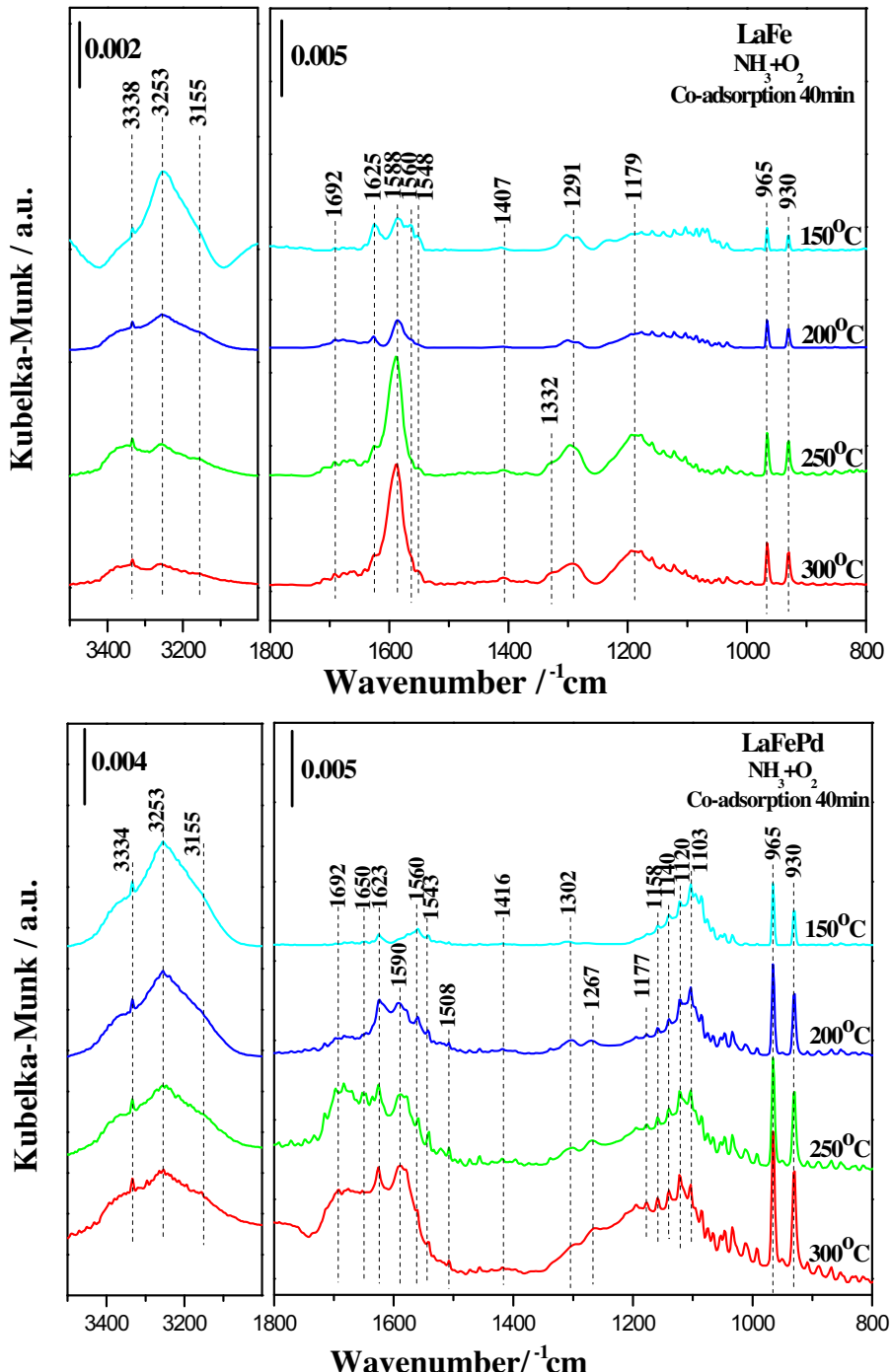


**Fig. 4.** DRIFT spectra recorded for: (a) LaFe, (b) LaFePd. Materials are exposed to 1000 ppm NH<sub>3</sub>, 1500 ppm O<sub>2</sub> in He and heated by step at temperatures between 150 °C and 300 °C.

palladium-containing perovskite is suggested to follow N<sub>2</sub>H<sub>x</sub> intermediate mechanism in which –NH<sub>2</sub> surface species, issued from NH<sub>3</sub> adsorption, form N<sub>2</sub>H<sub>x</sub> intermediate species which are further oxidized into N<sub>2</sub> or NO. The palladium, in the perovskite, allows to increase the surface concentration in N<sub>2</sub>H<sub>x</sub> intermediates.

### 3.7. DFT calculation

#### 3.7.1. Effect of Cu and Pd doping

Oxygen-vacancy-formation energy can be used as a mean to predict oxidation ability of oxygen containing surface. Lower energy

leads to easy loss of oxygen ions, that is beneficial for the surrounding oxygen atoms mobility [74]. The oxygen vacancy on LaFeO<sub>3</sub>, LaFe<sub>0.8</sub>Cu<sub>0.2</sub>O<sub>3</sub>, and LaFe<sub>0.95</sub>Pd<sub>0.05</sub>O<sub>3</sub> surfaces are generated when an oxygen atom is liberated from the surface, as represented in Fig. 5. According to the following equation:

$$E_v = E_{\text{defect}} + 1/2E_{\text{O}_2} - E_{\text{bulk}} \quad (4)$$

The oxygen vacancy formation energies (E<sub>v</sub>) of Cu-doped and Pd-doped samples are calculated to be 1.85 eV and 3.06 eV, respectively. This value is 2.18 eV for un-substituted LaFe sample (Table 1). Therefore, the introduction of Cu is beneficial to the formation of

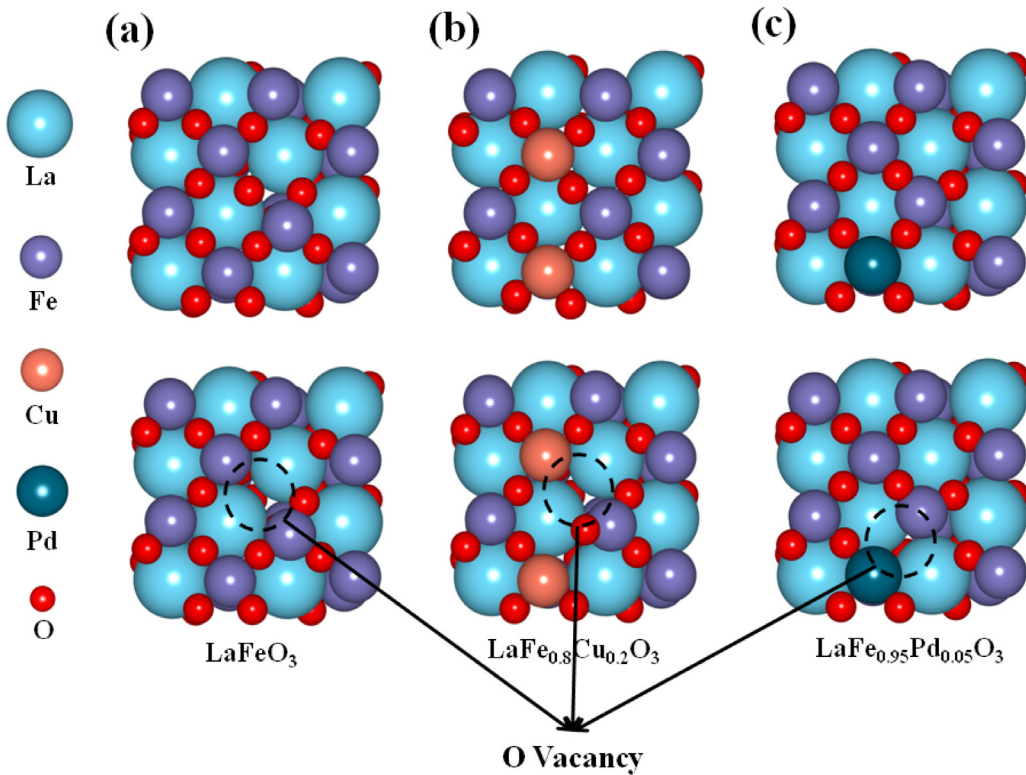
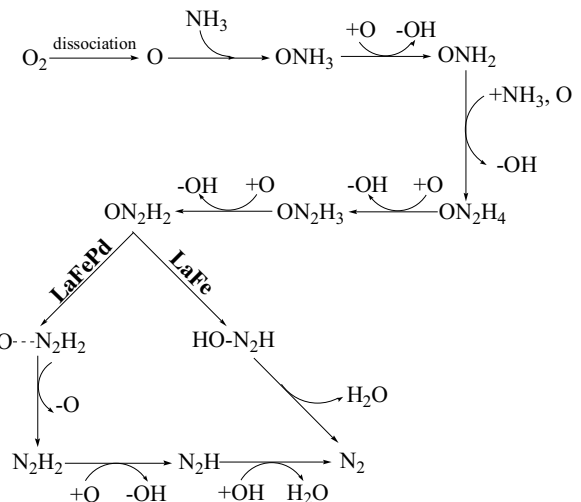


**Fig. 5.** Optimized structure calculated for bulk (a) LaFe, (b) LaFeCu, and (c) LaFePd, and corresponding oxygen vacancy formation on crystal surface.

oxygen vacancy and could thus improve the mobility/reactivity of surface oxygen atoms compared to LaFe. However, the introduction of Pd in the structure induces a negative effect on vacancies formation, and will consequently negatively impact oxygen mobility, which is in agreement with previously experimental data. [29] This result indicates, as experimentally observed in this study, that copper-containing perovskite is more efficient for total oxidation reaction than pure iron perovskite, while insertion of palladium is less effective for this issue than that of copper.

### 3.7.2. Reaction mechanism over $\text{LaFeO}_3$

To confirm  $\text{NH}_3$ -SCO reaction pathway over the surface of Fe-based perovskite as well as to identify how Pd-substitution influences the reaction mechanism, the free energy of the possible intermediates and transition states is calculated for each steps, by using density functional theory (DFT). Liu et al. [75] demonstrated that the surface Fe ions dominate the oxygen adsorption process, and the adsorbed  $\text{O}_2$  molecules over Fe ions are more stable than that over La ones. Moreover,  $\text{NH}_3$  molecules are preferably adsorbed on Fe-site or O-site, rather than on La-site because La belongs to alkaline elements. Therefore, the adsorption of molecular  $\text{O}_2$  and  $\text{NH}_3$  on  $\text{FeO}$  terminated  $\text{LaFeO}_3$  (0 1 0) surface is calculated to better understand the reaction pathway. The adsorption geometries are displayed in Fig. S8, and the calculated adsorption energies and atomic distances are summarized in Table S2. After calculation,  $\text{O}_2$  molecule is expected to preferentially adsorb at the surface of Fe-based perovskite, while  $\text{NH}_3$  molecule approaches the surface of sample with pre-adsorbed  $\text{O}_2$  molecule but does not directly coordinate on the surface (Fig. S5(d)), indicating that the reaction between pre-adsorbed  $\text{O}_2$  and  $\text{NH}_3$  from gas phase is difficult to occur. According to the early studies [76,77], O–O bond cleavage easily occurs on the surface of oxide. Based on the calculation results,  $\text{O}_2$  molecule dissociation did not need to overcome high energy barrier to produce active oxygen atoms. As shown in Fig. 6(a and b), the  $\text{O}_2$  adsorption energy is  $-1.62 \text{ eV}$ ,



**Scheme 1.** Proposed reaction network for the SCO of ammonia over LaFe and LaFePd perovskites.

and further surmount  $0.60 \text{ eV}$  to form bridged connection O–O structure. Subsequently, O–O bond scission takes place to obtain Fe-coordinated active oxygen atoms, with climbing energy barrier of  $1.44 \text{ eV}$ . These processes are described in Eqs. (5) and (6). Since  $\text{NH}_3$ -SCO reaction requires enough  $\text{O}_2$ , two  $\text{O}_2$  molecules are needed to be adsorbed on iron surface sites, to be further dissociated into four oxygen atoms, in order to be in accordance with the used reaction conditions (Scheme 1).



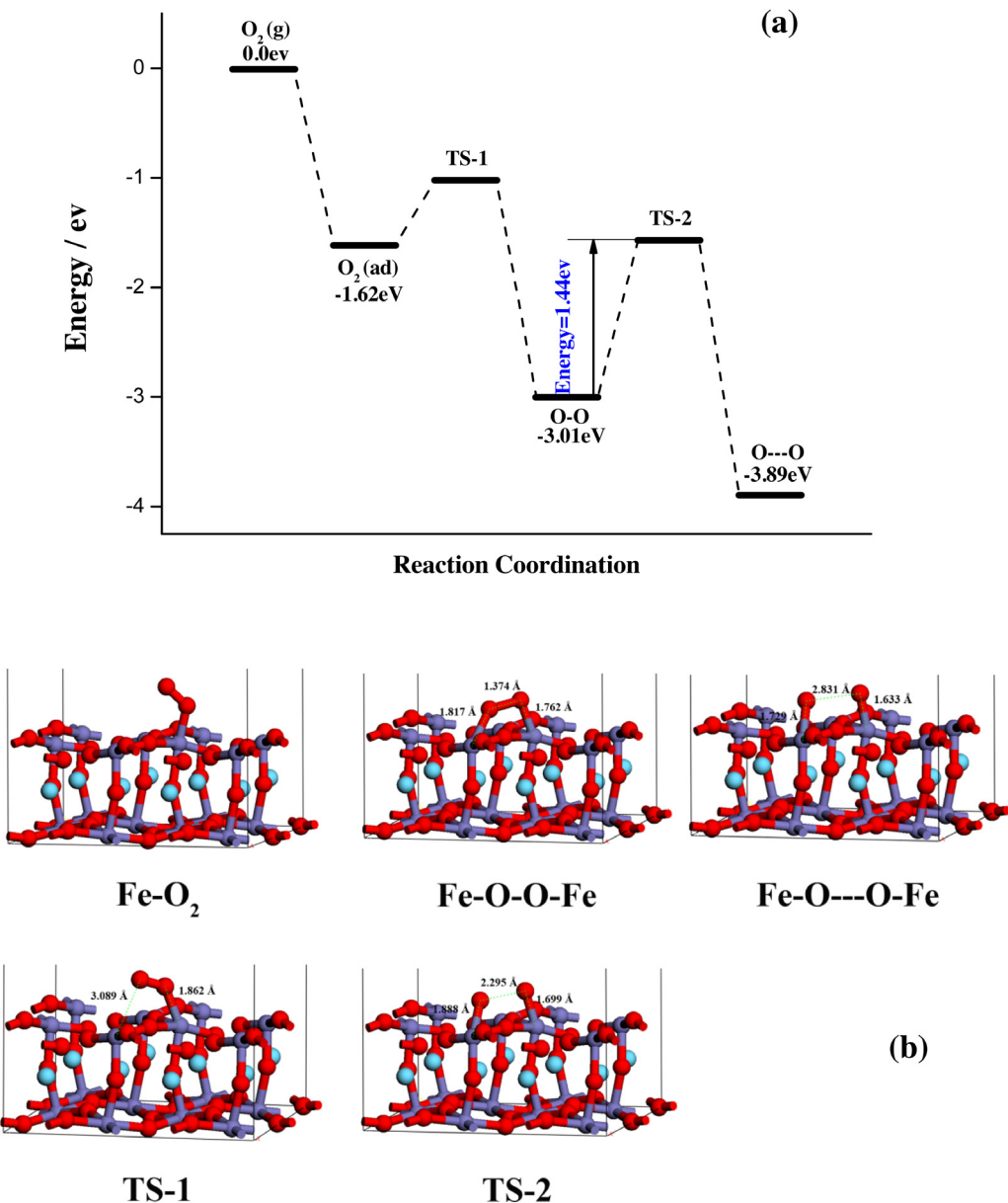
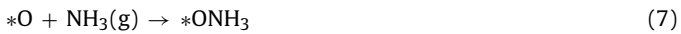


Fig. 6. Results of  $O_2$  dissociation reaction over  $LaFeO_3$  (0 1 0) surface: (a) Gibbs free energy profiles, (b) optimized geometries.

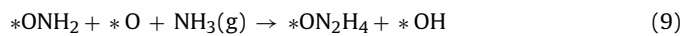
$NH_3$  adsorption, dissociation and  $N_2$  production process are also studied. The results on the Gibbs free energy profiles and optimized geometries are displayed in Fig. 7(a and b).  $NH_3$  molecule initially reacts with activated oxygen atoms to form  $-ONH_3$  species (IM1) (Scheme 1).  $Fe-O$  bond of  $1.860\text{ \AA}$ , and  $O-N$  bond of  $1.252\text{ \AA}$  are formed ( $E = -0.83\text{ eV}$ ). Thereafter, cleavage of the first  $N-H$  bond takes place to form hydroxylamine structure ( $-O-NH_2$ ). Reaction occurs between  $-ONH_3$  that combines with adjacent surface oxygen atom to generate  $-OH$  (mechanism associated with energy barrier of  $0.95\text{ eV}$ ; TS-1 in Fig. 7). These processes are described in Eqs. (7) and (8), and summarized in Scheme 1.



In this process,  $Fe-O$  bond shortens to  $1.831\text{ \AA}$  and  $O-N$  bond elongates to  $1.319\text{ \AA}$ , indicating that  $-NH_2$  species became reactive after dehydrogenation. The existence of stable  $-O-NH_2$  structure is consistent with *in-situ* DRIFTS results, while such observation was

already reported for V- and Co-based oxides [31,36]. Thereafter, two different processes can occur.

First,  $NH_3$ -SCO mechanism follows an Eley-Rideal (E-R) reaction pathway, during which gas phase  $NH_3$  reacts with surface  $-O-NH_2$  species. A second gas phase  $NH_3$  molecule can combine with adsorbed  $-O-NH_2$  species to produce stable  $-O-N_2H_4$  species (IM-3), including  $N-H$  fracture and  $H$  atom reaction with adjacent oxygen, with an energy of  $-0.92\text{ eV}$ .  $N-N$  bond length, in IM-3 species, is  $1.482\text{ \AA}$ . Subsequently, IM-3 species loses one  $H$  atom to produce  $-ON_2H_3$  (IM-4), with climbing an energy barrier of  $0.06\text{ eV}$  (TS-2). The next steps involve dehydrogenation, among which the step from  $-ON_2H_2$  (IM-5) to  $-OH-N_2H$  (IM-6) who needs to overcome the largest energy barrier ( $3.48\text{ eV}$ ). This reaction is identified as the rate-determining step in the whole chemical process to generate final  $N_2$  molecule. These last steps are described in Eqs. (9)–(12), and represented in Scheme 1.



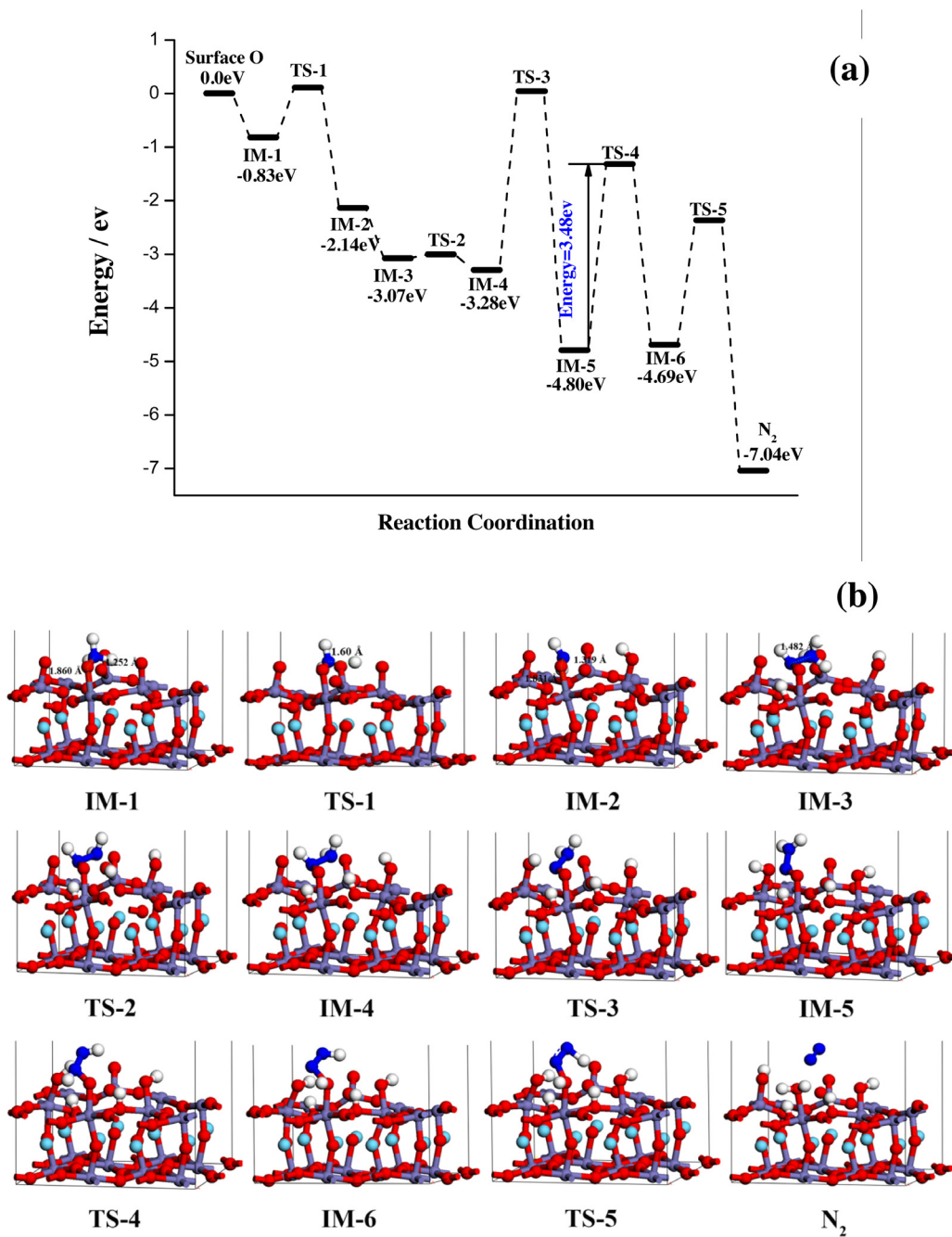
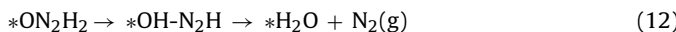


Fig. 7. Results of NH<sub>3</sub>-SCO reaction, to produce N<sub>2</sub>, by an E-R mechanism over LaFeO<sub>3</sub> (0 1 0) surface: (a) Gibbs free energy profiles, (b) optimized geometries.



Another possible reaction pathway could induce the formation of a second –ONH<sub>3</sub> species through NH<sub>3</sub> adsorption on surface sites, according to a Langmuir-Hinshelwood (L-H) reaction pathway (presented in Supplementary file, section S9). In this last case, reaction will proceed through adsorbed molecular species. Two adsorbed –ONH<sub>3</sub> surface species will react to produce diazo species (–N=N–) as depicted in Fig. S9. The reaction is considered as the rate-determining step, since a very high energy barrier of 7.04 eV needs to be surmounted to generate ON<sub>2</sub>H<sub>2</sub>O species (IM12). Consequently, NH<sub>3</sub>-SCO reaction is more likely to occur through an E-R mechanism that presents a significantly lower energy barrier to surmount than through a L-H mechanism. During E-R mechanism,

the rate-determining step is proposed to be the reaction between gaseous NH<sub>3</sub> and –O–NH<sub>2</sub> surface species to produce –ON<sub>2</sub>H<sub>4</sub> intermediate species.

### 3.7.3. Reaction mechanism over LaFe<sub>0.95</sub>Pd<sub>0.05</sub>O<sub>3</sub>

During the process of oxygen dissociation at the surface of the palladium substituted perovskite, O atom does not adsorb steadily at palladium surface site but migrates toward iron surface site (2.245 Å for Pd-O distance vs. 1.595 Å for Fe-O distance – Fig. 8). Pd<sup>2+</sup> incorporation on the material surface is observed to promote oxygen density around adjacent Fe-sites. Thereafter, NH<sub>3</sub> molecule prefers to adsorb on oxidized Fe-site rather than on reduced Pd-site. Interestingly, when gaseous NH<sub>3</sub> approaches the active surface oxygen, the first N–H cleavage takes place to form –ONH<sub>2</sub> (IM15), without climbing any energy barrier (Fig. 8). The second N–H bond

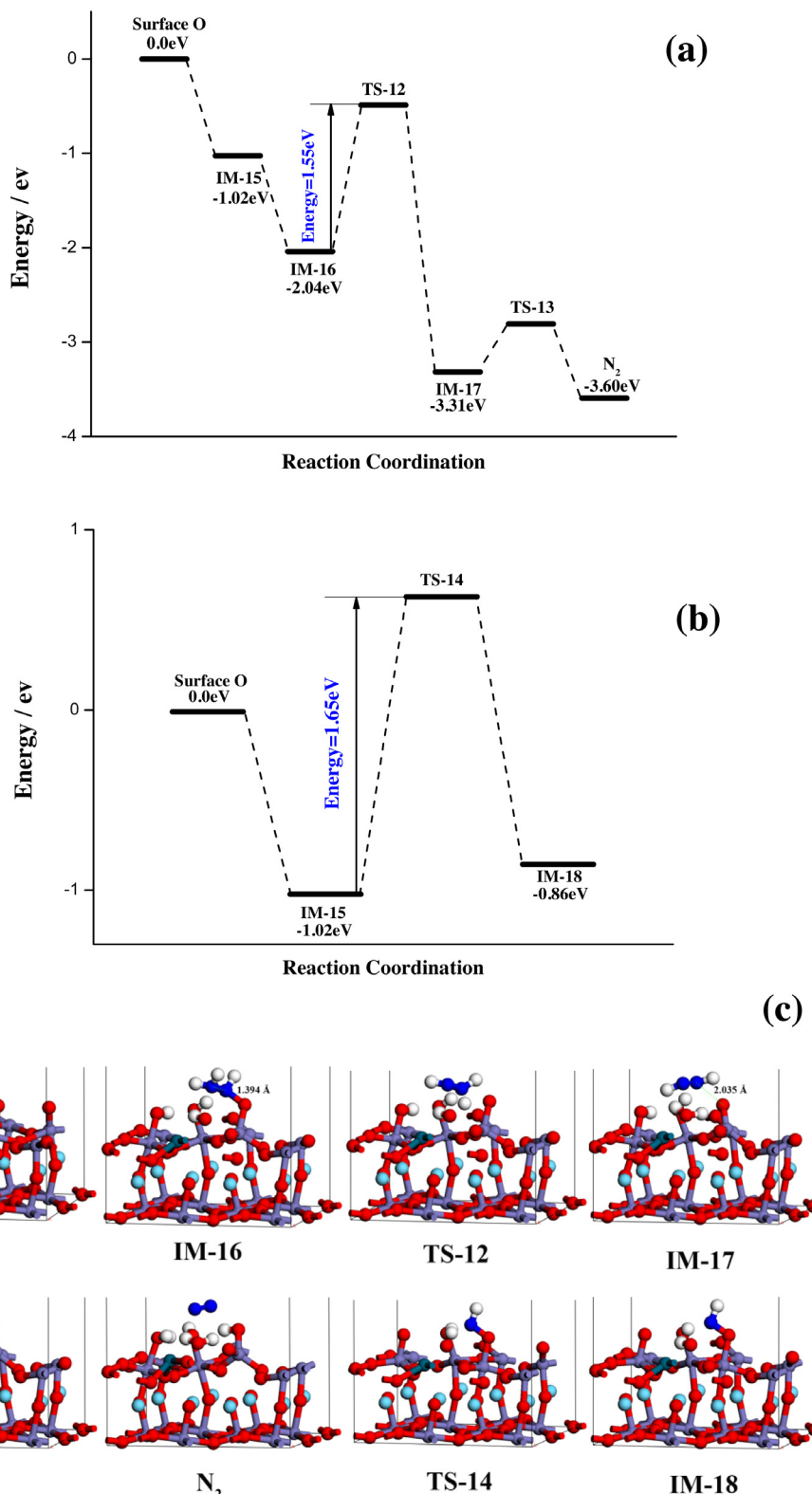
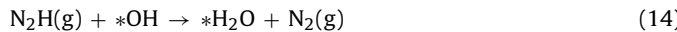


**Fig. 8.** Results of NH<sub>3</sub>-SCO reaction, to produce N<sub>2</sub>, by an E-R mechanism over LaFe<sub>0.95</sub>Pd<sub>0.05</sub>O<sub>3</sub> (0 1 0) surface: (a) and (b) Gibbs free energy profiles, (c) optimized geometries.

cleavage to form –ONH species shows energy barrier of 1.65 eV (Fig. 8(b)) compared to the first N–H cleavage, revealing that this process is unfavorable. As shown in Fig. 8(a), gaseous NH<sub>3</sub> will preferably react with –ONH<sub>2</sub> species to produce –ON<sub>2</sub>H<sub>3</sub> species (IM 16) with one N–H cleavage, which is similar to the reaction pathway observed at LaFeO<sub>3</sub> surface (Scheme 1). In addition, the

length of N=N bond (1.394 Å) in dimeric species (–N=N–) is shorter than that of N=N bond over LaFeO<sub>3</sub> surface (1.482 Å) indicating strong interactions between N atoms and high bond energy over Pd-doped sample. The adsorption energy required for this process is calculated at –1.18 eV, which is lower than over LaFeO<sub>3</sub>. Therefore, LaFePd sample possesses stronger affinity for NH<sub>3</sub> coupling,

as awaited from experimental results. Subsequently, the  $-\text{ON}_2\text{H}_3$  species further dehydrogenates. H atom can react directly with oxygen connected with N, or with *ortho*-position surface oxygen, to generate hydroxyl or  $\text{H}_2\text{O}$  molecule. It is worth noting that the O–N bond fracture is not difficult since an energy barrier of 1.55 eV (TS-12) is calculated. One H atom fall out during the step, forming  $-\text{N}_2\text{H}_2$  species (IM 17) with weak adsorption. The two last H removal can simultaneously take place, overcoming relatively low barrier energy of 0.51 eV (TS-13), to generate final  $\text{N}_2$  molecule as described in Eqs. (13) and (14), and as summarized in **Scheme 1**:



The rate-determining step is consequently O–N bond cleavage for LaFePd sample, while it is the  $-\text{O}–\text{N}_2\text{H}_2$  dehydrogenation to produce OH– $\text{N}_2\text{H}$  for LaFe sample (**Scheme 1**). This modification can originate from the surface weak oxygen mobility issued from palladium incorporation in the perovskite structure [29]. Also, in previous studies, Pd substitution was observed to strongly depress the production of surface ionic nitrate and promote N–O bond breakage, thus effectively enhancing the  $\text{N}_2$  yield [46,47]. Meanwhile, local oxygen density around Fe-site is enhanced by adjacent Pd doping, that is beneficial to the diazo species ( $-\text{N}=\text{N}-$ ) formation. Especially, at high temperature, superior oxygen mobility will facilitate N–H bond cleavage in  $-\text{ONH}$  species, resulting in higher NO yields. It may explain why NO yield for LaFe is higher than that of LaFePd sample.

#### 4. Conclusion

Selective catalytic oxidation of ammonia ( $\text{NH}_3$ -SCO) to nitrogen is studied over Fe-based perovskites ( $\text{LaFeO}_3$ ,  $\text{LaFe}_{0.8}\text{Cu}_{0.2}\text{O}_3$ , and  $\text{LaFe}_{0.95}\text{Pd}_{0.05}\text{O}_3$ ), and derived supported perovskites ( $\text{LaFe}_{0.8}\text{Cu}_{0.2}\text{O}_3/\text{Al}_2\text{O}_3$ , and  $\text{LaFe}_{0.95}\text{Pd}_{0.05}\text{O}_3/\text{Al}_2\text{O}_3$ ). The reaction pathway to form  $\text{N}_2$  has been investigated by a combination of *in-situ* DRIFTS and density functional theory (DFT) calculations over  $\text{LaFeO}_3$  and palladium-containing derived sample.  $\text{LaFeO}_3$  sample presents a limited reducibility, especially at low temperature. Cu and Pd substitutions are observed to enhance low temperature reducibility, resulting in better catalytic conversion for  $\text{NH}_3$  oxidation at low temperature. However, in the 300–600 °C temperature range,  $\text{N}_2$  yield is observed to decline over copper-substituted sample. This evolution is associated to the high oxygen mobility displayed by copper-containing solids that is in favor of N–H bond scission of adsorbed  $-\text{ONH}_3$  species, leading to high  $\text{NO}_x$  yield. By contrast, Pd-substituted sample presented excellent  $\text{NH}_3$  conversion, and even outstanding  $\text{N}_2$  yield in the 200–300 °C range. These excellent properties are originating from the limited oxygen mobility displayed by the palladium-doped material. Finally, amelioration of the catalytic properties, especially  $\text{N}_2$  yield at temperature above 300 °C, is achieved when perovskite phase is supported over alumina support. The best performances are obtained over  $\text{LaFe}_{0.95}\text{Pd}_{0.05}\text{O}_3/\text{Al}_2\text{O}_3$  that is presenting low light-off temperatures and high selectivity towards  $\text{N}_2$  over a wide temperature range (even at complete  $\text{NH}_3$  conversion).

Study of the  $\text{NH}_3$ -SCO mechanism evidenced that reaction pathway follows an Eley-Rideal pathway over Fe-based perovskites. The process involves the reaction between gaseous  $\text{NH}_3$  with adsorbed  $-\text{ONH}_2$  radical to obtain diazo species. For  $\text{LaFeO}_3$  material, the rate-determining step is calculated to be the  $-\text{ON}_2\text{H}_2$  to  $-\text{ON}_2\text{H}$  step (with an energy barrier of 3.48 eV), while for  $\text{LaFe}_{0.95}\text{Pd}_{0.05}\text{O}_3$ , the rate-determining step is identified as the O–N bond cleavage (with an energy barrier of 1.55 eV). Then, calculations evidence that palladium substitution favors N–O bond breakage, compared with what is obtained for unsubstituted material. This modifica-

tion effectively improves the  $\text{N}_2$  yield and reduce the  $\text{NO}_x$  yield in reaction.

#### Acknowledgments

S. Royer acknowledges Chevreul institute (FR 2638), Ministère de l'Enseignement Supérieur et de la Recherche, Région Nord – Pas de Calais and FEDER for funding.

#### Appendix A. Supplementary data

Supplementary data associated with this article can be found, in the online version, at <http://dx.doi.org/10.1016/j.apcatb.2016.10.021>.

#### References

- [1] C.-M. Hung, Powder Technol. 209 (2011) 29–34.
- [2] L. Chmielarz, M. Jabłońska, RSC Adv. 5 (2015) 43408–43431.
- [3] M. Jabłońska, R. Palkovits, Appl. Catal. B 181 (2016) 332–351.
- [4] J.N.A. Yuejin Li, Appl. Catal. B, 13 (1997) 131–139.
- [5] L. Zhang, C. Zhang, H. He, J. Catal. 261 (2009) 101–109.
- [6] S.D. Lin, A.C. Gluhoi, B.E. Nieuwenhuys, Catal. Today 90 (2004) 3–14.
- [7] R.Q.La.R.T. Yang, J. Catal., 201 (2001) 145–152.
- [8] G. Qi, R.T. Yang, Appl. Catal. A 287 (2005) 25–33.
- [9] S. Shrestha, M.P. Harold, K. Kamasamudram, A. Yezerski, Catal. Today 231 (2014) 105–115.
- [10] G. Qi, J. Catal. 226 (2004) 120–128.
- [11] C.-M. Hung, Powder Technol. 196 (2009) 56–61.
- [12] Z. Wang, Z. Qu, X. Quan, Z. Li, H. Wang, R. Fan, Appl. Catal. B 134–135 (2013) 153–166.
- [13] R.Q. Long, R.T. Yang, J. Catal. 207 (2002) 158–165.
- [14] A. Wöllner, F. Lange, H. Schmelz, H. Knözinger, Appl. Catal. A 94 (1993) 181–203.
- [15] G.R.L. Lietti, G. Busca, F. Bregani, P. ForzattiA, Catal. Today 64 (2000) 187–195.
- [16] N.I. Il'chenko, G.I. Golodets, J. Catal. 39 (1975) 57–72.
- [17] M. Jiang, B. Wang, Y. Yao, Z. Li, X. Ma, S. Qin, Q. Sun, Appl. Surf. Sci. 285 (Part B) (2013) 267–277.
- [18] Z. Wang, Z. Qu, X. Quan, H. Wang, Appl. Catal. A 411–412 (2012) 131–138.
- [19] X. Cui, L. Chen, Y. Wang, H. Chen, W. Zhao, Y. Li, J. Shi, ACS Catal. 4 (2014) 2195–2206.
- [20] S.M. Lee, H.H. Lee, S.C. Hong, Appl. Catal. A 470 (2014) 189–198.
- [21] J.-C. Lou, C.-M. Hung, S.-F. Yang, J. Air Waste Manag. 54 (2004) 68–76.
- [22] L. Chmielarz, P. Kuśtrowski, A. Rafalska-Łasocha, R. Dziembaj, Appl. Catal. B 58 (2005) 235–244.
- [23] L. Chmielarz, A. Węgrzyn, M. Wojciechowska, S. Witkowski, M. Michalik, Catal. Lett. 141 (2011) 1345–1354.
- [24] L. Chmielarz, M. Jabłońska, A. Strumiński, Z. Piwowarska, A. Węgrzyn, S. Witkowski, M. Michalik, Appl. Catal. B 130–131 (2013) 152–162.
- [25] C. Liang, X. Li, Z. Qu, M. Tade, S. Liu, Appl. Surf. Sci. 258 (2012) 3738–3743.
- [26] S. Song, S. Jiang, Appl. Catal. B 117–118 (2012) 346–350.
- [27] C.-M. Hung, J. Hazard. Mater. 180 (2010) 561–565.
- [28] C.-M. Hung, Powder Technol. 200 (2010) 78–83.
- [29] W. Yang, R. Zhang, B. Chen, N. Bion, D. Duprez, S. Royer, J. Catal. 295 (2012) 45–58.
- [30] R. Zhang, A. Villanueva, H. Alamdari, S. Kaliaguine, J. Catal. 237 (2006) 368–380.
- [31] R.-M. Yuan, G. Fu, X. Xu, H.-L. Wan, J. Phys. Chem. C 115 (2011) 21218–21229.
- [32] V.S.E. Jose Manuel, Gallardo Amoresa, Giang Guido Ramisb, Guido Buscab, Appl. Catal. B 13 (1997) 45–48.
- [33] G. Ramis, M. Angeles Larrubia, J. Mol. Catal. A 215 (2004) 161–167.
- [34] G.R.M. Angeles Larrubia, Guido Busca, Appl. Catal. B 30 (2001) 101–110.
- [35] S. Hong, A. Karim, T.S. Rahman, K. Jacobi, G. Ertl, J. Catal. 276 (2010) 371–381.
- [36] K. Shojaee, B.S. Haynes, A. Montoya, Appl. Surf. Sci. 316 (2014) 355–365.
- [37] C.-z. He, H. Wang, L.-y. Huai, J.-y. Liu, J. Phys. Chem. C 116 (2012) 24035–24045.
- [38] S. Royer, D. Duprez, F. Can, X. Courtois, C. Batiot-Dupeyrat, S. Laassiri, H. Alamdari, Chem. Rev. 114 (2014) 10292–10368.
- [39] R. Burch, J.P. Breen, F.C. Meunier, Appl. Catal. B 39 (2002) 283–303.
- [40] R. Zhang, H. Alamdari, S. Kaliaguine, Appl. Catal. B 72 (2007) 331–341.
- [41] R. Zhang, A. Villanueva, H. Alamdari, S. Kaliaguine, J. Mol. Catal. A 258 (2006) 22–34.
- [42] D.V. Ivanov, L.G. Pinaeva, L.A. Isupova, A.N. Nadeev, I.P. Prosvirin, L.S. Dovlitova, Catal. Lett. 141 (2010) 322–331.
- [43] D.V. Ivanov, E.M. Sadovskaya, L.G. Pinaeva, L.A. Isupova, J. Catal. 267 (2009) 5–13.
- [44] V. Blasin-Aubé, J. Belkouch, L. Monceaux, Appl. Catal. B 43 (2003) 175–186.
- [45] G. Peccati, P. Reyes, R. Zamora, L.E. Cadús, J.L.G. Fierro, J. Solid State Chem. 181 (2008) 905–912.
- [46] R. Zhang, H. Alamdari, S. Kaliaguine, J. Catal. 242 (2006) 241–253.

[47] W. Yang, R. Zhang, B. Chen, D. Duprez, S. Royer, *Environ. Sci. Technol.* 46 (2012) 11280–11288.

[48] D. Sellam, M. Bonne, S. Arrii-Clacens, G. Lafaye, N. Bion, S. Tezkratt, S. Royer, P. Marécot, D. Duprez, *Catal. Today* 157 (2010) 131–136.

[49] M. Bonne, N. Bion, F. Pailloux, S. Valange, S. Royer, J.M. Tatibouet, D. Duprez, *Chem. Commun.* (2008) 4504–4506.

[50] M. Bonne, D. Sellam, J.P. Dacquin, A.F. Lee, K. Wilson, L. Olivi, A. Cognigni, P. Marecot, S. Royer, D. Duprez, *Chem. Commun.* 47 (2011) 1509–1511.

[51] R. Zhang, W. Yang, N. Luo, P. Li, Z. Lei, B. Chen, *Appl. Catal. B* 146 (2014) 94–104.

[52] T. Das, S.-C. Kweon, J.-G. Choi, S.Y. Kim, I.-H. Oh, *Int. J. Hydrogen Energy* 40 (2015) 383–391.

[53] T. Asada, T. Kayama, H. Kusaba, H. Einaga, Y. Teraoka, *Catal. Today* 139 (2008) 37–42.

[54] P. Courty, H. Ajot, C. Marcilly, B. Delmon, *Powder Technol.* 7 (1973) 21–38.

[55] S. Royer, D. Duprez, S. Kalaguique, *J. Catal.* 234 (2005) 364–375.

[56] Z. Qu, H. Wang, S. Wang, H. Cheng, Y. Qin, Z. Wang, *Appl. Surf. Sci.* 316 (2014) 373–379.

[57] F. Benaliouche, Y. Boucheffa, P. Ayrault, S. Mignard, P. Magnoux, *Microporous Mesoporous Mater.* 111 (2008) 80–88.

[58] G. Olofsson, L. Reinewallenberg, A. Andersson, *J. Catal.* 230 (2005) 1–13.

[59] L.I. Darvell, K. Heiskanen, J.M. Jones, A.B. Ross, P. Simell, A. Williams, *Catal. Today* 81 (2003) 681–692.

[60] Y. Zhang, D. Wang, J. Wang, Q. Chen, Z. Zhang, X. Pan, Z. Miao, B. Zhang, Z. Wu, X. Yang, *Chin. J. Catal.* 33 (2012) 1448–1454.

[61] M.A. Al-Daous, A.A. Manda, H. Hattori, *J. Mol. Catal. A* 363–364 (2012) 512–520.

[62] P. Xiao, L. Zhong, J. Zhu, J. Hong, J. Li, H. Li, Y. Zhu, *Catal. Today* 258 (2015) 660–667.

[63] M.D. Salazar-Villalpando, D.A. Berry, A. Cugini, *Int. J. Hydrogen Energy* 35 (2010) 1998–2003.

[64] V. Albaladejo-Fuentes, F.E. López-Suárez, M.S. Sánchez-Adsuar, M.J. Illán-Gómez, *Appl. Catal. A* 488 (2014) 189–199.

[65] X. Li, C. Chen, C. Liu, H. Xian, L. Guo, J. Lv, Z. Jiang, P. Vernoux, *ACS Catal.* 3 (2013) 1071–1075.

[66] A. Glisenti, M. Pacella, M. Guiotto, M.M. Natile, P. Canu, *Appl. Catal. B* 180 (2016) 94–105.

[67] R. Zhang, P. Li, R. Xiao, N. Liu, B. Chen, *Appl. Catal. B* 196 (2016) 142–154.

[68] M.G. Rosmaninho, J.C. Tristão, F.C.C. Moura, R.M. Lago, M.H. Araújo, J.L.G. Fierro, *Anal. Bioanal. Chem.* 396 (2010) 2785–2795.

[69] G. Olofsson, A. Hinz, A. Andersson, *Chem. Eng. Sci.* 59 (2004) 4113–4123.

[70] A. Akah, C. Cundy, A. Garforth, *Appl. Catal. B* 59 (2005) 221–226.

[71] W. Chen, Y. Ma, Z. Qu, Q. Liu, W. Huang, X. Hu, N. Yan, *Environ. Sci. Technol.* 48 (2014) 12199–12205.

[72] T. Nanba, S. Masukawa, J. Uchisawa, A. Obuchi, *Appl. Catal. A* 419–420 (2012) 49–52.

[73] R. Zhang, N. Luo, W. Yang, N. Liu, B. Chen, *J. Mol. Catal. A* 371 (2013) 86–93.

[74] B. Liu, J. Liu, S. Ma, Z. Zhao, Y. Chen, X.-Q. Gong, W. Song, A. Duan, G. Jiang, *J. Phys. Chem. C* 120 (2016) 2271–2283.

[75] X. Liu, J. Hu, B. Cheng, H. Qin, M. Zhao, C. Yang, *Sens. Actuators B: Chem.* 139 (2009) 520–526.

[76] W.F.S., Hangyao Wang, David Schmidt, *J. Phys. Chem. C* 113 (2009) 15266–15273.

[77] X.-L. Xu, W.-K. Chen, J.-q. Li, *J. Mol. Struct. Theochem.* 860 (2008) 18–23.